Analysis of Shape Memory Properties in 3D Printed PLA

A Major Qualifying Project Submitted to the Faculty of Worcester Polytechnic Institute in partial fulfillment of the requirement for the Degree in Bachelor of Science in Mechanical Engineering

By

_____

Tsering Dolma

_____

Andrew Kelly

_____

Jesse Kauffman

_____

Emily Perkins

Date: 03/23/2018

Project Advisors:

_____

Professor Amy M. Peterson

Abstract

In recent years, 3D printing has become a popular alternative to conventional manufacturing techniques; untapped potential exists for application of 3D printing across various industries. However, additional research on 3D printing technology is still required in order to produce accurate results and to be able to apply the technology to a wide range of industries. This research focuses on verifying relationships between printing parameters and thermal strain accumulated in 3D printed polylactic acid (PLA). Results from raster angle and layer thickness strain experiments were fit to an algorithm for predicting irreversible thermal strain. While experimental data trends agreed with theory in certain cases, magnitudes of strain deviated significantly from expected values. Such deviations required alteration of the set of algorithm equations. This research provides crucial initial steps for future research in developing an accurate method for predicting strain in Material Extrusion (MatEx) printed PLA parts.

Acknowledgements

We would like to extend our thanks to Professor Amy M. Peterson and Anthony D'Amico for their instruction and support during our work on this MQP. We would also like to thank Worcester Polytechnic Institute for providing us with the opportunity and resources to fulfill this project.

Table of Contents

List of Figures

List of Tables

1. Introduction

Material extrusion (MatEx) is a common form of additive manufacturing (AM) that creates objects by depositing roads of polymer, layer by layer. During this process, stresses build up within layers due to differences in coefficients of thermal expansion (CTE), and quick cooling of deposited layers. Shape memory polymers (SMP) occur as a result of residual stresses within a material. When a certain activation process, such as annealing, is applied to the material, it experiences deformation as a release of strain. Other shape memory materials include alloys and ceramics; shape memory polymers are lightweight and less expensive in comparison, making them advantageous for certain applications. SMPs have practical applications in the medical, dental, automobile, aerospace, and construction industries. For example, self-deploying capsules for drug delivery activated by the temperature inside the human body, replacement of metal wires in orthodontic braces with SMPs, deformation recovering automobile coatings to minimize damage in collisions, and self-deploying solar sails for space systems are all applications of interest with SMPs [1-3].

With knowledge of the effects of various printing parameters on internal stresses, it is possible to predict strain that occurs in parts. The scope of this research was focused on one-way shape memory properties of polylactic acid (PLA). An existing printing algorithm for predicting thermal strain was modified, and further developed to create a toolbox of PLA-based SMP applications. The algorithm was modified by relating layer thickness, outline shells, raster angle and properties of PLA to thermal strain in parts. The following aims have been carried out in order to accomplish this objective.

Aim 1: Modify and validate an algorithm for achieving accurate 3D printed structure dimensions

Aim 2: Observe shape transformations of PLA structures after annealing

Aim 3: Study effects of outline shell thickness on irreversible thermal strain

The modified algorithm was used to predict shape memory transformations of PLA structures; accuracy of printed results were evaluated. With further development, the resultant, optimized 3D printing technique could be applied in the creation of an engineering toolbox made up of elongating, shrinking, expanding, bending, and twisting SMP structures. These SMP functions could be applied to the design of highly accurate 3D printed pin fixtures with applications as tamper-evident, and self-tightening fasteners.

2. Background

2.1 History of additive manufacturing

Three-dimensional (3D) printers are machines that create complex 3D structures from user-created Computer Aided Design (CAD) models. Historically, these printers have been used for rapid prototyping, but, in recent years, manufacturing of end-use, customizable parts for practical applications has increased [4]. The practice of 3D printing has grown in popularity due to the low cost and level of expertise required to use this technology [5].

2.2 Detailed description of material extrusion process

Relative to conventional manufacturing techniques, MatEx is inexpensive and can be faster than techniques that require extensive retooling. However, achievable precision of this technique is limited. This explains why MatEx is most commonly utilized for rapid prototyping rather than for creating final parts [6]. Polymers such as acrylonitrile butadiene styrene (ABS) and PLA are the most commonly used materials for MatEx primarily due to their availability, price, and compatibility with the MatEx process [7].

To print parts with a 3D printer, a CAD design file is converted into an .stl file, and then into GCode using slicing software. GCode is a machine language that commands the way a 3D printer, as well as other computer numerical control (CNC) machines, moves to create a sliced .stl file. The extruder of a MatEx printer deposits material in a prescribed pattern in the X and Y axes while the build plate moves in the Z axis, allowing layers of material to be printed on top of each other. During MatEx, a polymer filament spool is fed through guide tubes into a heated chamber within the print head (Figure 1).

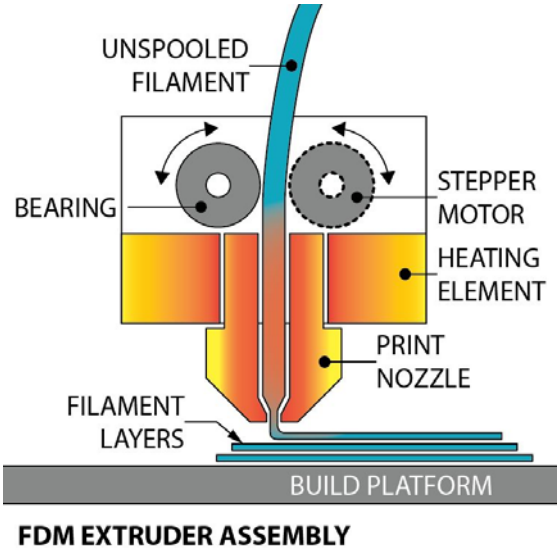

Figure 1: Illustration of extrusion process [8]

The chamber heats the polymer filament until it reaches sufficient viscosity for flow, typically within a range of 195-255 °C, and extrudes it onto the build plate where the filament cools and solidifies [9]. Once concluded, MatEx results in a multilayer structure [10].

2.2.1 Printing parameters

As use of AM has grown, a range of 3D printers have been created for both industrial and individual manufacturing purposes. Brands currently on the market include MakerBot, Stratasys, Ultimaker, Zortrax, and Formlabs [11]. Slicing software and 3D printer model determine the amount of control a user has over customizing properties and parameters, including infill percentage, layer thickness, extruder nozzle temperature, extruder speed, raster angle, build plate temperature, cooling fan speed, and number of outline shells. These customizations allow various levels of resolution, structural features, and mechanical properties to be achieved.

2.2.2 Residual stresses in MatEx

MatEx structures have been shown to exhibit irreversible thermal strain that leads to warping upon annealing above glass transition temperature (T_g) [12-13]. However, even pre-anneal, MatEx parts exhibit large residual stresses that lead to layer delamination and warping. Past research has determined relationships between certain printing parameters and the properties of irreversible thermal strain through deformation in printed parts. For example, analysis of layer thickness and raster angle has been utilized to predict residual stress in printed parts that cause irreversible thermal strain [12]. It was found that larger strain occurs at lower layer thickness. Strain direction changed as raster angle increased from 0° to 90° in the X and Y axes [13]. At 0° raster angle, roads are printed parallel to the X axis and perpendicular to the Y axis; at 90° raster angle, roads are printed parallel to the Y axis and perpendicular to the X axis. The strain in the Z axis was independent of raster angle [13]. Shear strain showed an inverse parabolic trend with largest strain observed at 45° raster angle [13].

2.2.3 MatEx material selection

MatEx printers are designed to heat and extrude thermoplastic materials to build parts. Thermal and mechanical properties such as T_g, shear modulus (G), coefficient of thermal expansion (CTE), and crystallinity are critical considerations when choosing a material for MatEx [9,14,15]. These material characteristics are crucial in describing flow behavior of materials during MatEx and residual stress development during cooling. MatEx is a high shear process; a large shear modulus will make the material more viscous with lower shear rates, which will cause it to exhibit larger deformation during extrusion and greater die swell upon print [16]. Die swell is a phenomenon that occurs in polymer extrusion when extrudate diameter is greater than the size of the extrusion nozzle. This causes polymer strands to stretch while traveling through the nozzle, before relaxing upon extrusion.

Crystallinity and CTE may be important factors to consider when observing internal stresses developed during printing. While the crystallinity of MatEx materials affects internal stresses accumulated in parts by mitigating strains that occur, MatEx may be too rapid a process

for crystallinity to be a factor in residual stress buildup. An amorphous polymer structure allows greater polymer chain mobility compared to a crystalline structure; greater chain mobility allows more strain to occur in polymers [17]. This effect would occur when annealing MatEx parts, not when printing. Printing temperature is much greater than T_m of a polymer, and so extruded material is in an amorphous state, having no crystal structure. Polymers with a semi-crystalline structure exhibit both amorphous and crystalline regions and so will have properties of both amorphous and crystalline structures [16].

Commercially available polymers used in MatEx include thermoplastics such as PLA, ABS, polyvinyl alcohol (PVA), Nylon, polycarbonate, high impact polystyrene (HIPS), polyethylenimine (PEI), and chlorinated polyethylene (CPE) [9]. Differences in structure and material properties of these polymers affect resulting properties and internal stresses in parts. The thermal properties discussed above are compared between PLA and ABS in Table 1. CTEs reported in Table 1 signify values for a range of temperatures.

Table 1: Comparison of thermal properties of ABS and PLA relevant to 3D printing [18]

Comparison of Thermal Properties of Polymers		
Property	ABS (Extruded)	PLA (General Use)
Glass transition temperature [°C]	88-120	52-60
Thermal conductivity [W/m.°C]	0.226-0.235	0.13-0.16
Specific heat capacity [J/kg.°C]	1.39e3-1.41e3	1.13e3-1.21e3
Coefficient of thermal expansion [µstrain/°C]	108-150	126-145

2.3 Residual stress and irreversible thermal strain

An important factor considered in the design of MatEx parts is accumulation of residual stress during printing [19]. Residual stresses are internal stresses that remain in MatEx parts after a part has been printed, and has cooled. Presence of residual stress decreases the performance of MatEx parts, and can lead to structure failure in real world applications [20]. Stress developed in parts is, to some extent, due to non-uniform thermal gradients common during MatEx [19]. Newly extruded layers contract during cooling; some contraction is restricted by previously deposited layers that have already cooled [12,21]. This implies that prevented contraction of newly deposited layers increases residual thermal stress within fabricated parts.

One technique used for reducing residual stresses is to anneal finished parts above T_g [21]. When printed polymer parts are annealed, residual stresses are released through thermal strain [20-21]. During annealing, thermal strain as much as 27 times greater was observed. From this, it can be surmised that T_g does not largely contribute to stress relieved during annealing. Residual stresses build as the temperature of extruded filament cools to ambient temperature because, below T_g, filament hardens and residual stress can no longer be released [22].

Development of residual stress is heavily dependent on process parameters such as layer thickness, and raster orientation [12,20]. D'Amico et al. showed that irreversible thermal strain increases as layer thickness decreases. Built-in thermal stress observed at layer interfaces, and rapid cooling rates contribute to this [12, 22]. In terms of raster orientation, residual stresses built

up in the direction of extruded roads because contraction upon cooling is more restricted along the length of a road, rather than perpendicular to the road [12]. Relationships between residual stress and irreversible thermal strain, as well as the role of process parameters on the accumulation of residual stress, can be used to build a more controlled process for printing polymers with specific shape memory behavior.

2.4 Process used to predict irreversible strain in ABS

Previous research suggested that forces driving strain may build up in the direction of printed roads [12-13]. In a previous MQP report, *One-Way 3D Printed Shape Memory Polymers*, the relationship between raster angle and layer thickness on irreversible thermal strain was analyzed in order to create an algorithm for predicting the degree of strain in annealed parts [12]. The algorithm consisted of four equations calculating strain in the X axis, Y axis, Z axis and X-Y shear plane. Equations were derived from Hooke's law for an isotropic, homogeneous material undergoing tri-axial stress (Equations 1-4).

$$\varepsilon_x = \frac{1}{E} * [\sigma_x - \nu_{xy}(\sigma_y + \sigma_z)] \quad \textbf{(Equation 1)}$$

$$\varepsilon_y = \frac{1}{E} * [\sigma_y - \nu_{xy}(\sigma_z + \sigma_x)] \quad \textbf{(Equation 2)}$$

$$\varepsilon_z = \frac{1}{E} * [\sigma_z - \nu_z(\sigma_x + \sigma_y)] \quad \textbf{(Equation 3)}$$

$$\gamma_{xy} = \frac{\tau_{xy}}{G} \quad \textbf{(Equation 4)}$$

These equations were used as a model to develop the algorithm [10]. The algorithm and how it can be incorporated with experiments is further discussed in the methodology section.

2.4.1 One way shape memory polymer applications

Shape memory polymer parts have the ability to be "pre-programmed" with a specific shape so that the part will change into its intended form by applying a stimulus (heat, electrical impulses, chemical energy, or radiation) [23]. This function makes them versatile tools for various applications; SMPs have been applied to many fields for uses such as fixation, deployable structures, and actuation in both macroscopic and microscopic biosensors/systems [24]. Currently, the medical field uses SMPs for large implantable devices such as meshes in compressed forms, sutures, and artificial muscles [25-26]. Lendlein et al. explains that a future application of biodegradable thermoplastic as sutures would allow for more precise force by tightening when raised above a transition temperature [26]. As more research is done to improve SMPs, the range of uses for this technology will grow.

3. Methodology

3.1 Calibrate algorithm for achieving accurate part dimensions

To achieve dimensional accuracy of annealed, 3D printed designs, strain data from 3D printed PLA samples was fit to an algorithm (Equations 5-8).

$$\varepsilon_x = (F_r/(\ E * w_r * l_t)) * (cos^2(\theta) - v_{xy}sin^2(\theta)) \quad \textbf{(Equation 5)}$$

$$\varepsilon_y = (F_r/(\ E * w_r * l_t)) * (sin^2(\theta) - v_{xy}cos^2(\theta)) \quad \textbf{(Equation 6)}$$

$$\varepsilon_z = (F_r/(\ E * w_r * l_t)) * (-v_z) \quad \textbf{(Equation 7)}$$

$$\gamma_{xy} = (F_r/(\ G * w_r * l_t)) * sin(\theta) * cos(\theta) \quad \textbf{(Equation 8)}$$

This algorithm, based on Hooke's Law of plane and shear stress, calculates strain, ε_x, ε_y, ε_z, on a printed part in the X, Y, and Z axes as well as the shear strain, γ_{xy}, in the X-Y plane. F_r, E, w_r, and l_t represent axial force on printed roads, elastic modulus of the printed material, road width, and layer thickness, respectively. Variables θ, υ_{xy}, and υ_z represent raster angle, Poisson's ratio between X and Y axes, and Poisson's ratio perpendicular to the layer plane. Assuming constant road width, this printing algorithm was tested with ABS and found successful at predicting ε_x and ε_y, but limited in predicting magnitude of ε_z and γ_{xy} [13].

3.2 Sample Printing

Samples were printed with XYZ dimensions of 15mm x 10mm x 30mm using natural color PLA filament manufactured by 3D Universe. Part designs were created using SolidWorks; .stl files of designs were imported to Ultimaker Cura slicer software to be converted to G-Code. Samples were printed in groups of six. All parts were printed using an Ultimaker 3 3D printer with 70% infill density, an extruder temperature of 230°C, a print speed of 80 mm/s, and build plate temperature of 60°C.

Printing parameters were chosen in the "Custom" print setup menu in Cura (Figure 2). Throughout the experiment, samples were printed at varying layer thicknesses, and raster angles. The raster angle of samples were controlled by setting the infill pattern for each layer of a part to "line," and the line angle to the desired raster angle.

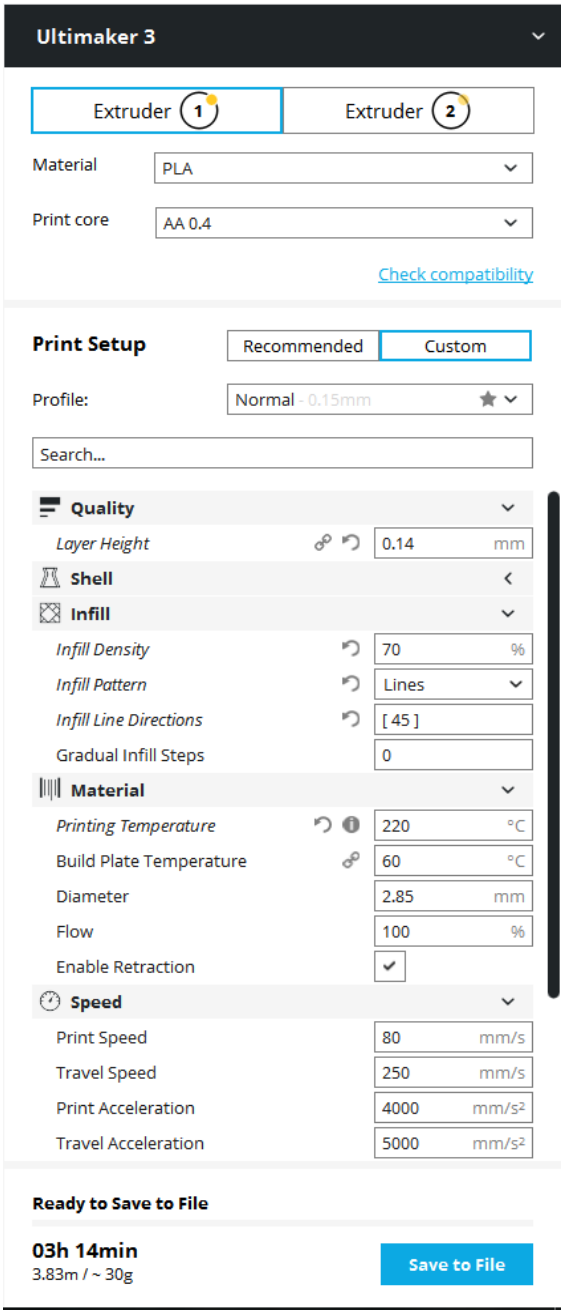

Figure 2: Custom print setup menu in Cura

3.3 Measuring PLA Samples

Once printed, samples were labeled with layer thickness and raster angle. Each set was grouped in a separate plastic bag to keep parts organized. Parts were measured with digital calipers with a 0.01mm accuracy. Dimensions in the X and Y axes were measured at three points; one measurement at the bottom of the sample about 5mm from the bottom, one measurement at the midpoint, and one measurement about 5mm from the top of the sample (Figure 3).

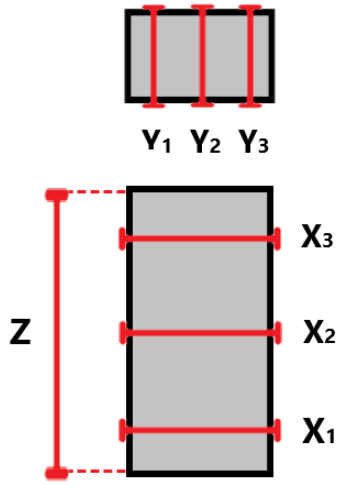

Figure 3: Bottom, mid and top measuring points of parts in the X and Y axes

The XY cross-section of many annealed samples warped into a rectangular shape that was rounded along the longer sides. Post-annealed samples were consistently measured with the calipers in the same fashion as the pre-annealed samples, parallel to the sides of each part after 24 hours of cooling time (Figure 4).

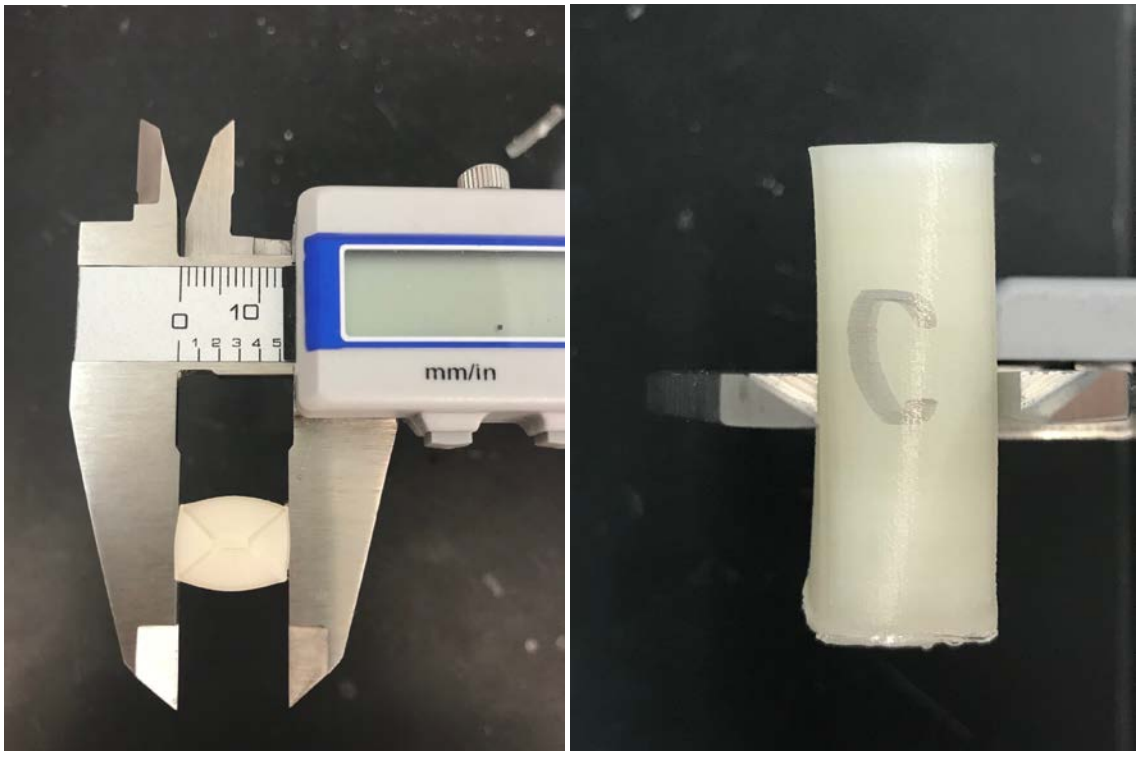

Figure 4: Illustration of points of measure parallel to sample sides in the X-dimension

3.4 Differential Scanning Calorimetry Test of PLA

In order to determine the T_g in printed PLA samples, Differential Scanning Calorimetry (DSC) was conducted using a Netzsch Polyma DSC 214. 9.8 mg of a printed sample, placed in a crucible, was used as the test sample. The reference was an empty crucible. During the test, samples were heated from 25℃ to 150℃ at a rate of 10℃/min in the presence of nitrogen gas. A maximum temperature of 150℃ was chosen because it was known to be well above T_g [18]. The sample and reference were cooled, and then went through the heating and cooling cycle a second time. T_g was determined by locating the endothermic elbow for the two cycles on a heat flow rate vs. temperature plot.

3.5 Annealing PLA Samples

To determine the annealing time to fully relieve residual stress, six sample groups of five parts each were annealed for different lengths of time. Samples were created with identical nominal dimensions and printing parameters. Each sample group was annealed in a Thermo/Precision Scientific 25EM Laboratory Oven approximately 15℃ above T_g. DSC testing determined T_g to be 62℃; therefore samples were annealed at about 77℃. In the oven, samples were placed on firebricks, as previous research indicated the bricks reduced warping caused by uneven heating from the oven bed [13]. One sample group was annealed for each length of time: 10 minutes, 30 minutes, 1 hour, 2 hours, 5 hours, and 10 hours. Once removed from the oven, samples were left to cool at room temperature for 24 hours to ensure no changes in resultant strain would take place after measurements were taken. Dimensions were then recorded and strain was calculated for each annealing time. An example of a possible shape transformation is shown in Figure 5. Results were used to determine when parts had reached their maximum deformation, which was defined as the optimal anneal time.

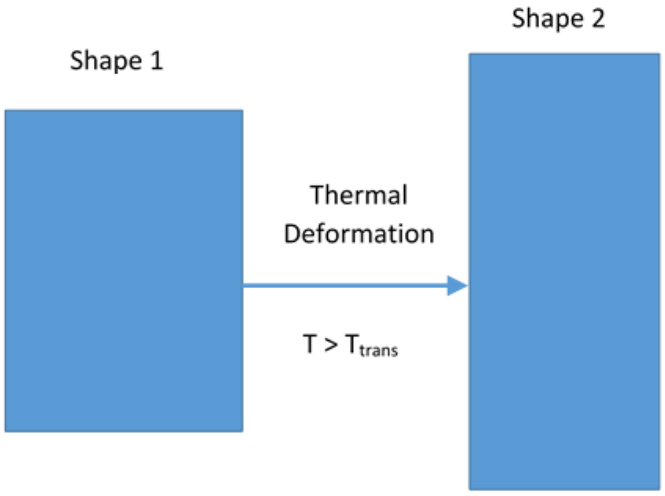

Figure 5: Example shape deformation: elongation in Z axis and shrinkage in X and Y axes

3.6 Validation and Refinement of Algorithm

Once the optimal anneal time for PLA samples was determined, five sample sets were printed at different raster angles, one each at 0°, 30°, 45°, 60°, and 90°, all with 140µm layer thickness. Additionally, four sample sets were printed at different layer thicknesses, one each at 40µm, 70µm, 100µm, and 300µm, all with 45° raster angle. Sample sets were measured pre- and post-annealing. Each set was annealed for the previously determined optimal annealing time of 5 hours. X, Y, and Z axis strains were calculated using pre- and post-annealing dimensions of each sample. Shear strain resulting from annealing was determined by analyzing shear angle with ImageJ. Angle (ϕ), indicated in Figure 6, is the complementary angle to the shear strain. ϕ was measured with the labeled side of the sample facing up, ensuring all samples were measured at the same orientation. Using Equations 5-8 with strain data from sample sets, a least squares fitting method was used to determine terms F_r/E, ν_{xy} and ν_z values.

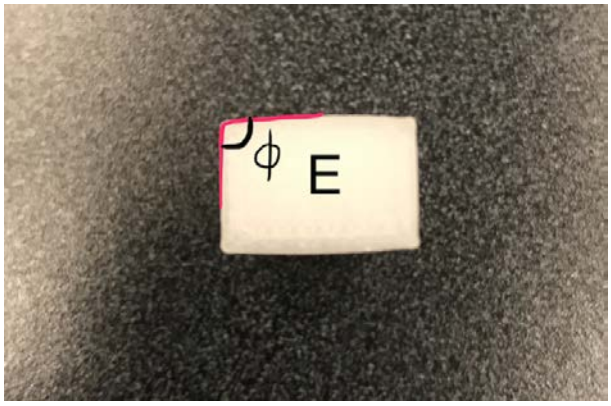

Figure 6: Angle of sample measured

If data did not fit theoretical strain predicted by the algorithm, equations of the algorithm were altered. In previous research, the algorithm was validated by printing ABS. To account for differences between previous theoretical expectations of ABS and data collected for PLA, constants and/or functions of variables were added to algorithm equations until empirical strain closely matched experimental strain.

Once strain output by the algorithm was able to predict experimental strain, a set of four samples were printed, annealed, and measured in order to further validate the algorithm. Desired dimensions (L_x, L_y, L_z), raster angle and layer thickness were input into the altered algorithm equations to calculate initial dimensions. Initial design dimensions output from the algorithm are shown in Table 3.

Table 2: Final printing dimensions for PLA parts to evaluate printing algorithm

Dimension	Value
L_x	20 mm
L_y	20 mm
L_z	20 mm
γ	1.78°

Table 3: Printing dimensions and parameters for PLA test parts to evaluate printing algorithm

L_{x0} [mm]	L_{y0} [mm]	L_{z0} [mm]	Printing Raster Angle [°]	Printing Layer Thickness [mm]
21.7	20.8	18.8	45°	0.14

Accuracy of printed parts was evaluated by observing dimensional change of samples after annealing. Results were deemed successful when parts achieved dimensional accuracy within 5% of desired design values and shear strain data were within an acceptable deviation of 0.50°. Unsuccessful validation indicated that the algorithm needed adjustment for use with PLA.

3.7 Observing Effect of Outline Shells on Shape Transformation

In order to gain a better understanding of the effects of outline shells on resultant strain, five outline shell thicknesses, ranging from 1mm to 5mm, were tested. These numbers were selected in order to create five equally distributed data points between the standard infill of 1mm and the maximum possible infill of 5mm. Strain and volumetric changes in each sample were calculated. A design of experiments (DOE) was created using JMP software to determine the minimum sample groups necessary for this experiment. The experiment involved printing five sample sets of consisting of six samples each.

Table 4: Print strategy to analyze effect of outline shell thickness on annealed PLA

Sample Set	Initial Printing Dimensions (X,Y,Z) mm	Raster Angle (°)	Layer Thickness (µm)	Shell Thickness (mm)
1	15, 10, 30	45	60	1
2	15, 10, 30	45	60	2
3	15, 10, 30	45	60	3
4	15, 10, 30	45	60	4
5	15, 10, 30	45	60	5

4. Results

4.1 Determine Optimal Annealing Time

Time to complete irreversible shape transformation, herein referred to as optimal annealing time, was determined by annealing specimens over a range of times and measuring the resulting changes in dimensions. Results, shown in Figure 7, demonstrate irreversible shape transformation due to annealing.

A t-test of average strain indicated that the effect of additional annealing time was negligible after five hours. The p-value (0.375) was greater than the p-critical value (0.05), meaning that the null hypothesis was not rejected. Therefore, five hours was the shortest amount of time to reach full annealing and was selected as the annealing time for all subsequent studies.

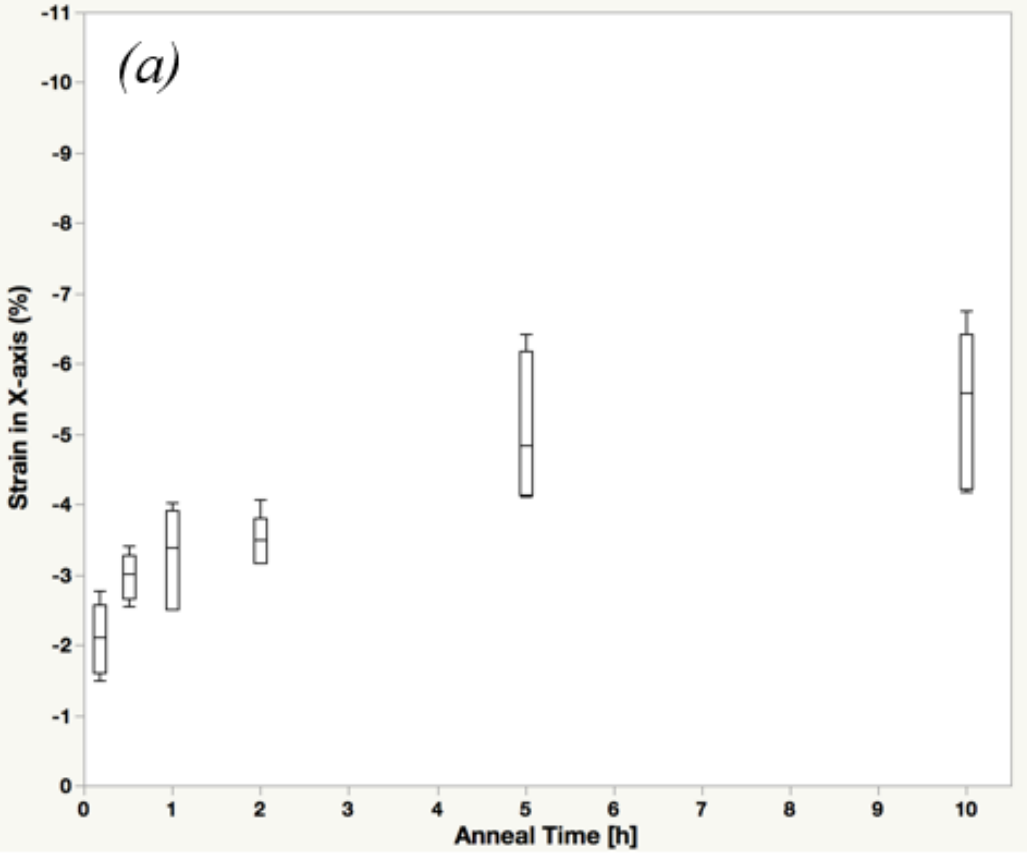

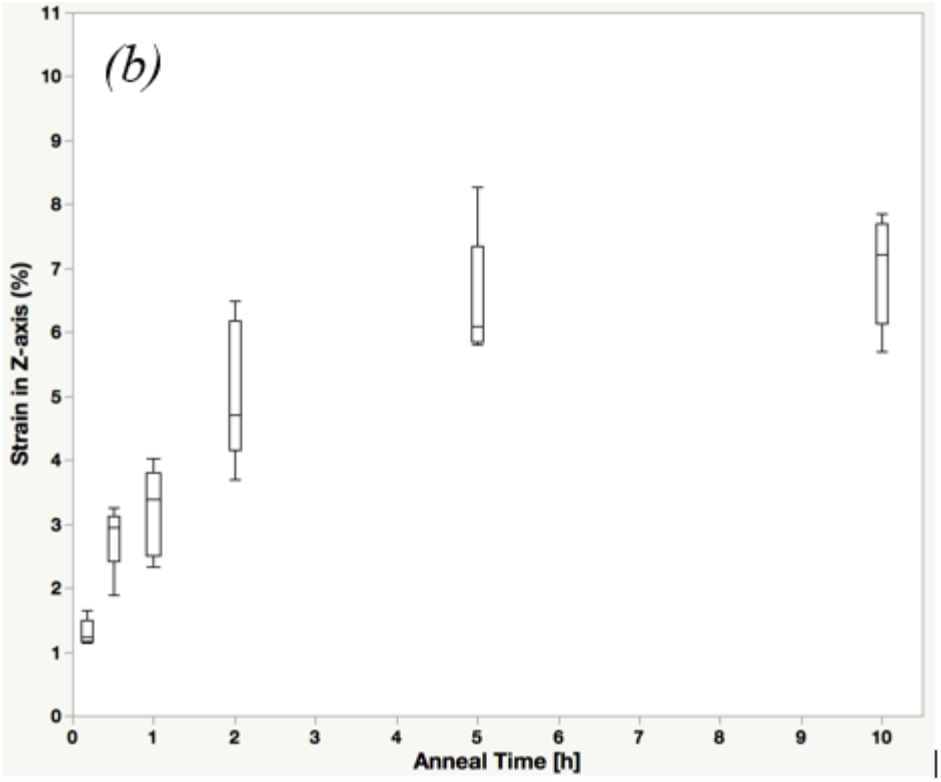

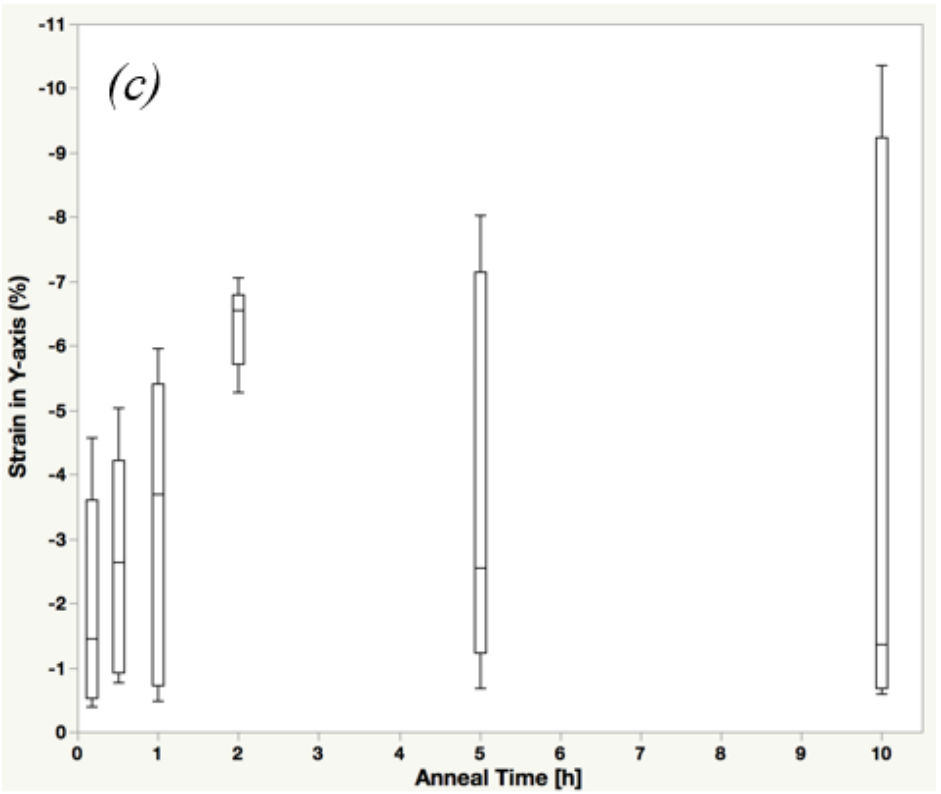

Figure 7: (a) X axis (b) Z axis (c) Y axis Strain vs. Anneal Time

4.2 Effect of Layer Thickness

Decreasing layer thickness of samples printed with the same dimension resulted in greater total number of layers. Previous research showed that irreversible thermal strain increases with decreasing layer thickness [12]. Collected data shows an inverse relationship between layer thickness and magnitude of irreversible strain (Figure 8), agreeing with the trend observed in previous research.

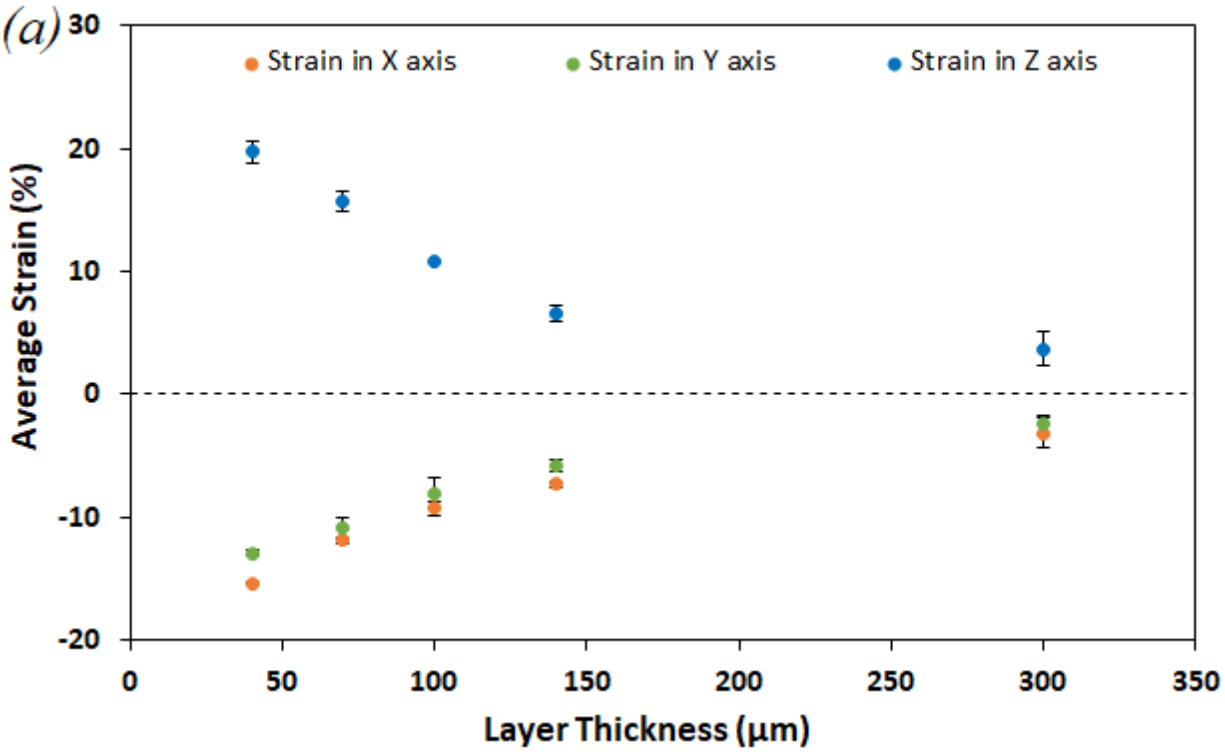

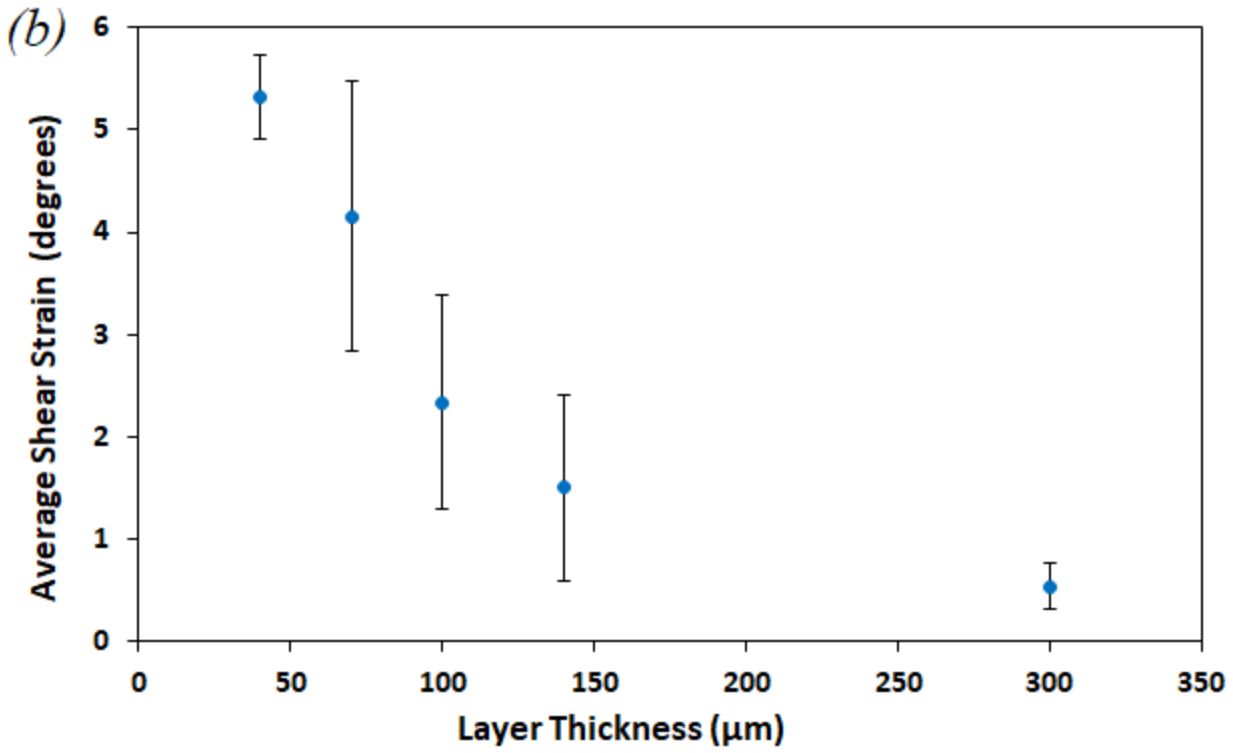

Figure 8: Measured Average Strain vs. Layer Thickness at 45° in a) X, Y, and Z axes b) Shear plane with error bars representing standard deviation of mean strain of sample set

4.3 Effect of Raster Angle

Previous research has shown that raster angle effects direction of strain [12]. Data gathered coincides with this, as show in Figure 9 (a) and (b). At a 0° raster angle, roads are printed parallel to the X axis, and perpendicular to the Y axis. Forces acted parallel to roads, so maximum strain in the X axis and minimum strain in the Y axis were expected at 0° raster angle; conversely, maximum strain in the Y axis and minimum strain in the X axis occurred at 90° raster angle [13]. A t-test shows that, with a p-value of 0.189, X axis strain observed at 0° and 30° raster angles do not statistically significantly differ. Experimental Y axis strain displayed expected trends seen in previous research [13].

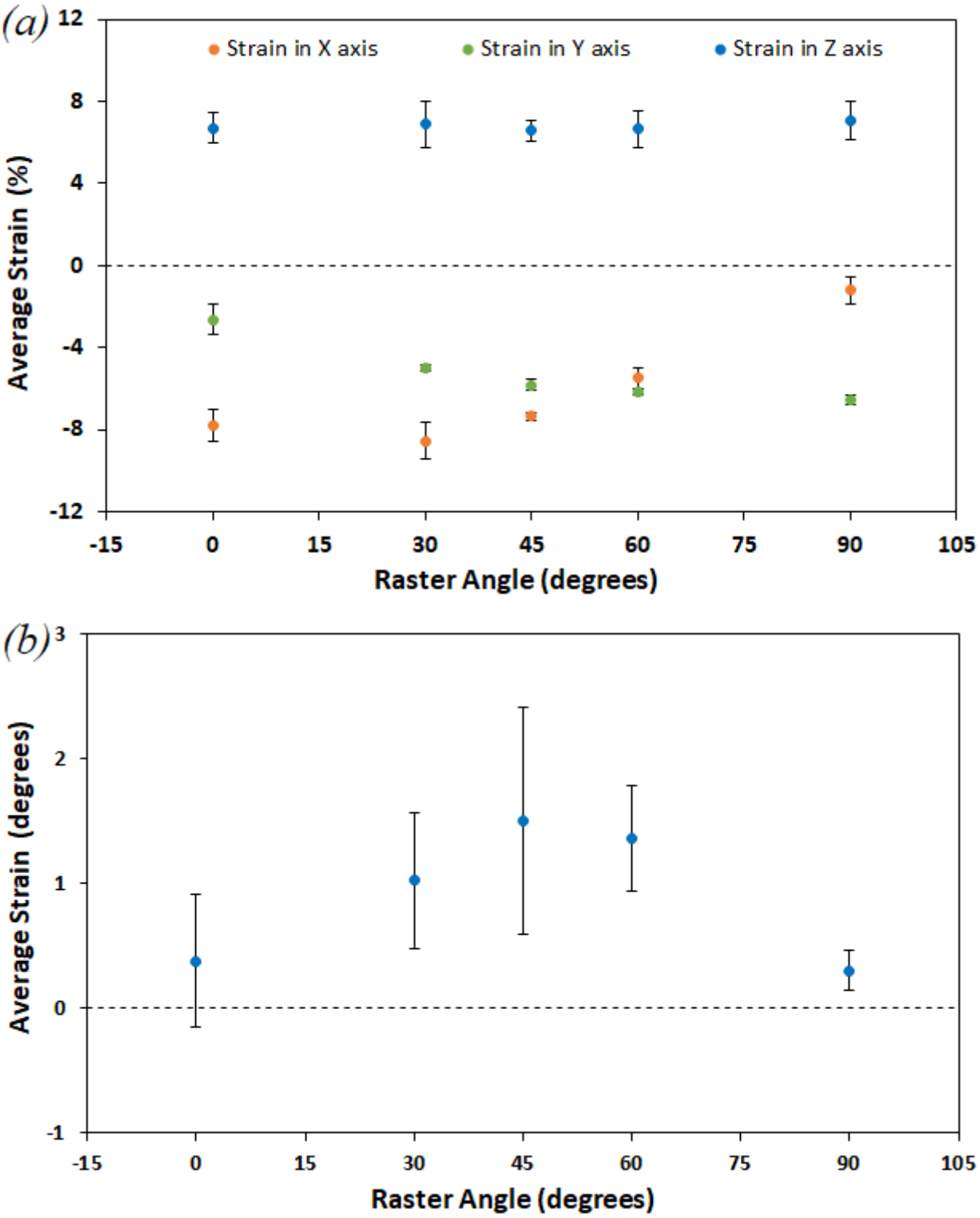

Figure 9: Measured Average Strain vs. Raster Angle at a layer thickness of 140µm in a) X, Y, and, Z axes b) shear plane with error bars representing standard deviation of mean strain of sample set

Z axis strain was found to be independent of raster in previous studies [12]. Experimental strain in the Z axis exhibited a relatively straight line trend. One-way ANOVA of strain values at each raster angle gave a p-value of 0.912. This p-value is substantially greater than the alpha, p = 0.05, meaning that strain values were not statistically significantly different and Z axis strain was independent of raster angle in PLA.

As expected, maximum shear strain was observed at 45° raster angle, when shear force is greatest. Additionally, minimum shear strain was observed at 0° and 90° (Figure 9b). However, shear strain was expected to be zero at these angles [13].

4.4 Fitting Data to Algorithm

Variables F_r/E, ν_{xy} and ν_z in Equations 9-12 were fit using least squares fitting.

$$\varepsilon_x = (F_r/(\,E * w_r * l_t)) * (cos^2(\theta) - v_{xy}sin^2(\theta)) \quad \textbf{(Equation 9)}$$

$$\varepsilon_y = (F_r/(\,E * w_r * l_t)) * (sin^2(\theta) - v_{xy}cos^2(\theta)) \quad \textbf{(Equation 10)}$$

$$\varepsilon_z = (F_r/(\,E * w_r * l_t)) * (-v_z) \quad \textbf{(Equation 11)}$$

$$\gamma_{xy} = (F_r/(\,G * w_r * l_t)) * sin(\theta) * cos(\theta) \quad \textbf{(Equation 12)}$$

Variables ε, F_r, E, w_r, l_t, and G, represent the strain, road force, modulus of elasticity, road width, layer thickness, and shear modulus, respectively. Poisson's ratio, ν_{xy} and ν_z, represent the ratio between the negative of strain in one axis, and strain in a perpendicular axis. A negative Poisson's ratio between the X and Y axes indicates that strain in the X axis occurred in the same direction as strain in the Y axis. Fitted values are shown in Table 5.

Table 5. Values of fitted variables in strain prediction algorithm

Variable	Fitted Value
Fr/E	-5.51×10^{-9}
ν_{xy}	-1.31
ν_z	0.657

Calculation of ν_{xy} values, using experimental data at each raster angle, ranged from -5.43 to -0.18. Therefore, the fitted value for ν_{xy} is consistent with observed strain. A positive ν_z is consistent with observed relations between X or Y, and Z strain. Calculated values for ν_z using experimental data range from 0.17 to 1.24. Thus, magnitude of the fitted value is logical.

Output from Equations 5-8 are compared with measured strain in all axes (Figures 10-13). Data in certain axes fit more closely than others.

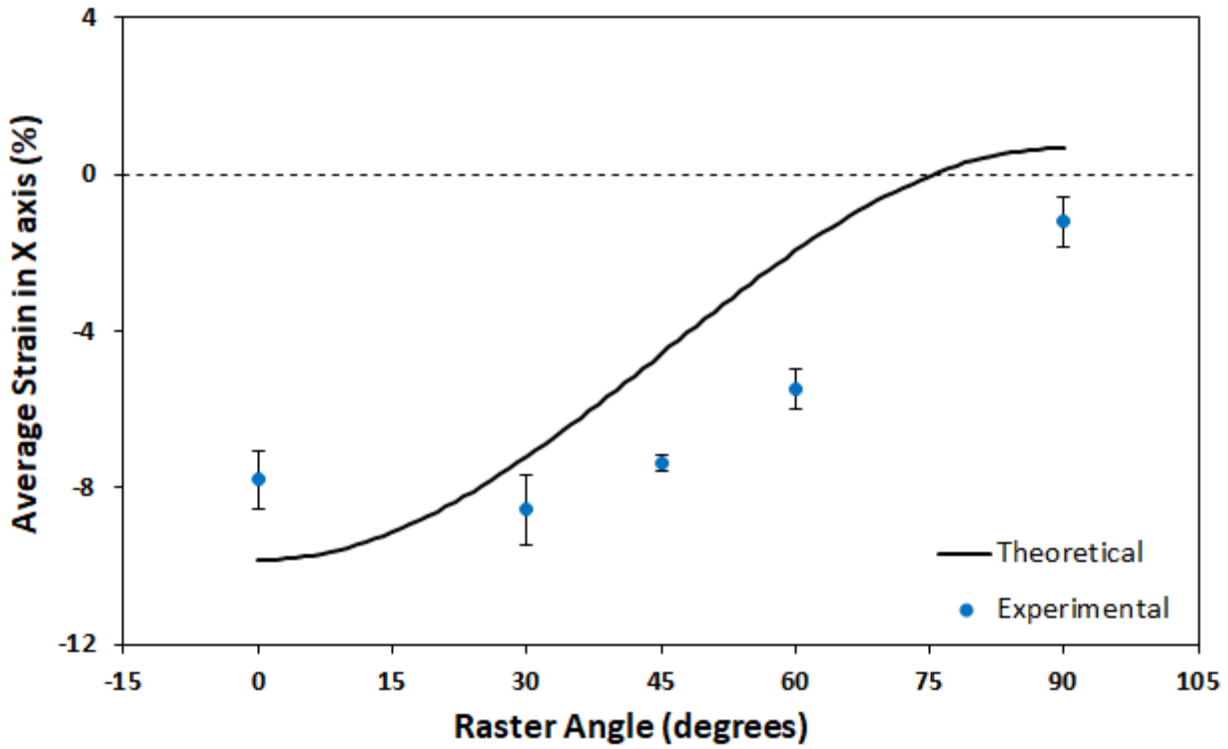

Figure 10: Calculated vs Measured Strain at 140µm in X axis with error bars representing standard deviation of mean strain of sample set

Although the experimental trend of X axis data (Figure 10) is consistent with the theoretical trend, the majority of strain magnitudes were larger than expected values. A detailed discussion regarding the discrepancy between experimental and theoretical data can be found in the following paragraphs.

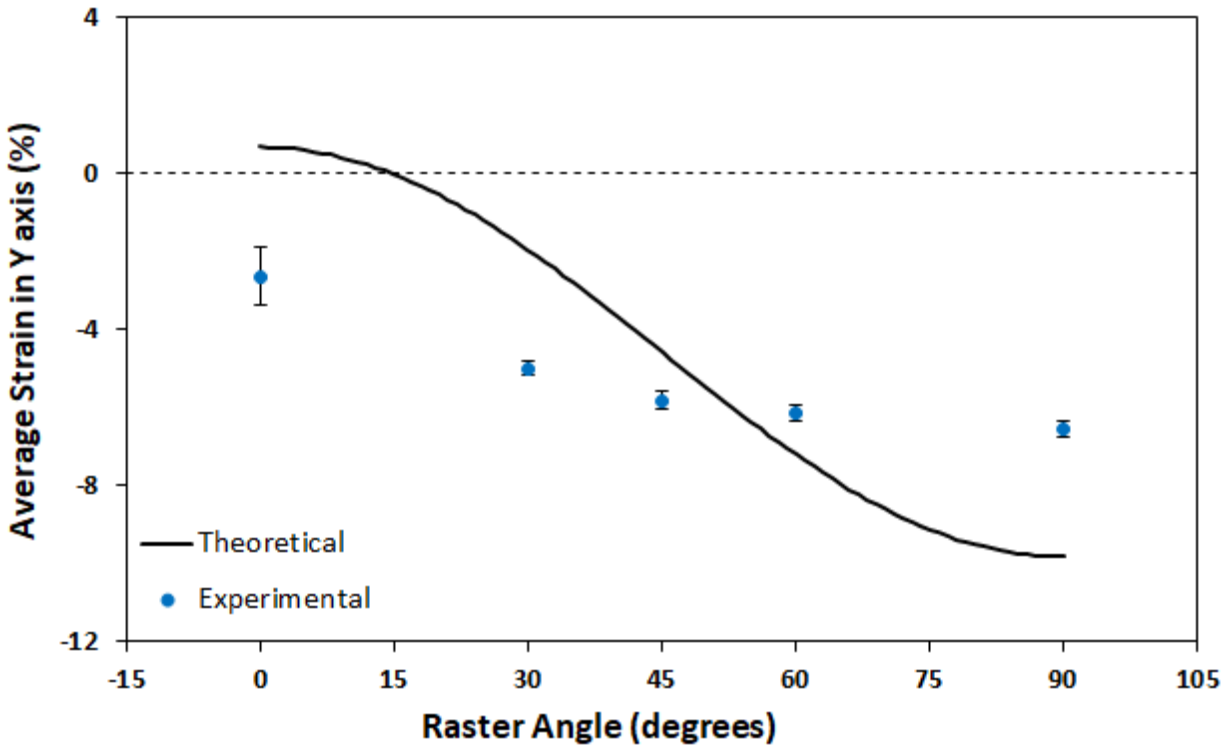

Figure 11: Calculated vs Measured Strain at 140µm in Y axis with error bars representing standard deviation of mean strain of sample set

Theoretical strain in the Y axis relating to raster angle does not agree with the relationship observed in experimental results (Figure 11). Although an increasing trend in strain is shown, strain magnitude wasn't as large as expected. Large deviation of theoretical strain from experimental results in the Y axis cannot be attributed to random error. Warping observed in samples appeared as rounded bulges that were especially distinct on the XZ-surface (Figures 4 and 12). Difficulties inherent in measuring the rounded bulges in warped sections of samples could be a source of error in strain data of annealed samples.

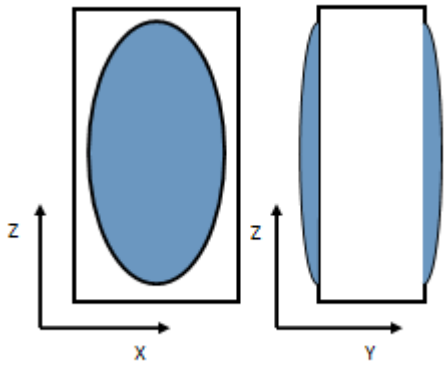

Figure 12: Warping in the XZ-Plane

Warping was most apparent in the Y axis; therefore, errors in measurement were most prevalent in the Y axis. Among sample sets of annealed layer thickness samples, warping had a consistent effect on the shape of samples (Figure 14a,b). Warping of raster angle samples, however, did not have the same consistent effect (Figure 14c,d). Due to this, layer thickness samples were easier to measure without including warping. Raster angle samples were measured as consistently as possible. However, warping, which occurred at the edge of samples, may have had an effect on raster angle data (Figure 9a). Warping may also have occurred differently between experiments due to the temperature at which samples were annealed. Raster angle sample sets were annealed at approximately 77°C, while layer thickness sample sets were annealed at approximately 80°C. This difference may have had an effect on the magnitude of strain measured.

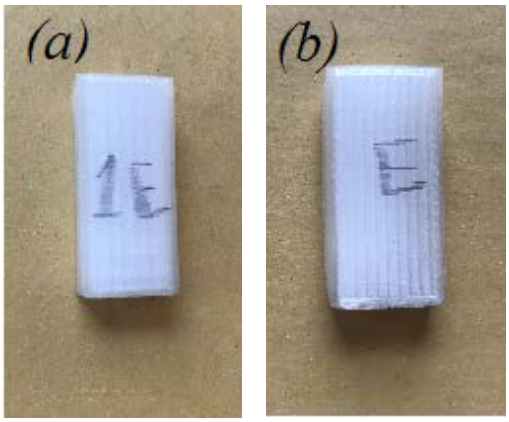

Figure 13: Difference between samples printed at a) 0° raster angle b) 90° raster angle

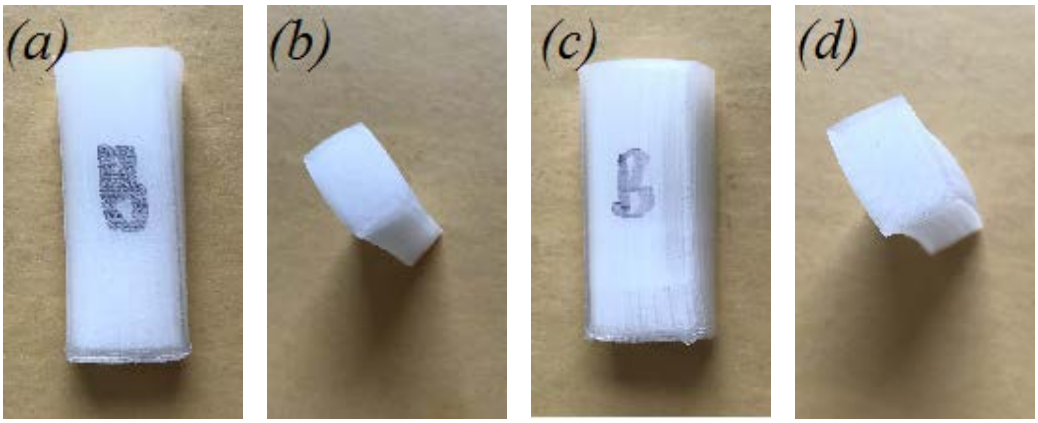

Figure 14: Difference in warping between layer thickness and raster angle samples a) front and b) side view printed at layer thickness of 40µm c) front and d) side view printed at 60° raster angle

In future experiments, annealing temperature should be the same for all sample sets to achieve better consistency. Bulges can also be avoided by measuring along the edges of parts without having the calipers cross the center of the sample. The current method for measuring temperature inside the oven is with a mercury thermometer; temperature may have been misread as the thermometer had to be pulled to the front of the oven to read, during which time the temperature value may have decreased. Another factor that could be contributing to differences in

data are material properties of PLA. The stiffness of PLA is lower than that of ABS, indicated by a comparison of flexural moduli of the two materials (3.1-3.6GPa for PLA and 1.2-2.8GPa for ABS) [18]. Low stiffness makes warping more apparent perpendicular to the XZ-plane of samples [18].

The algorithm was designed to be generalizable among polymers, and has been validated with ABS, an amorphous polymer. However, the algorithm had previously not been tested with a semi-crystalline polymer such as PLA [13]. Inhibited strain due to crystallinity could produce results with strain values of smaller magnitude than expected. This is not the case for all deviations in the X and Y axes; it is likely that measurement error due to warping in samples also contributed to this deviation, producing different variations in strain values from theoretical at different raster angles.

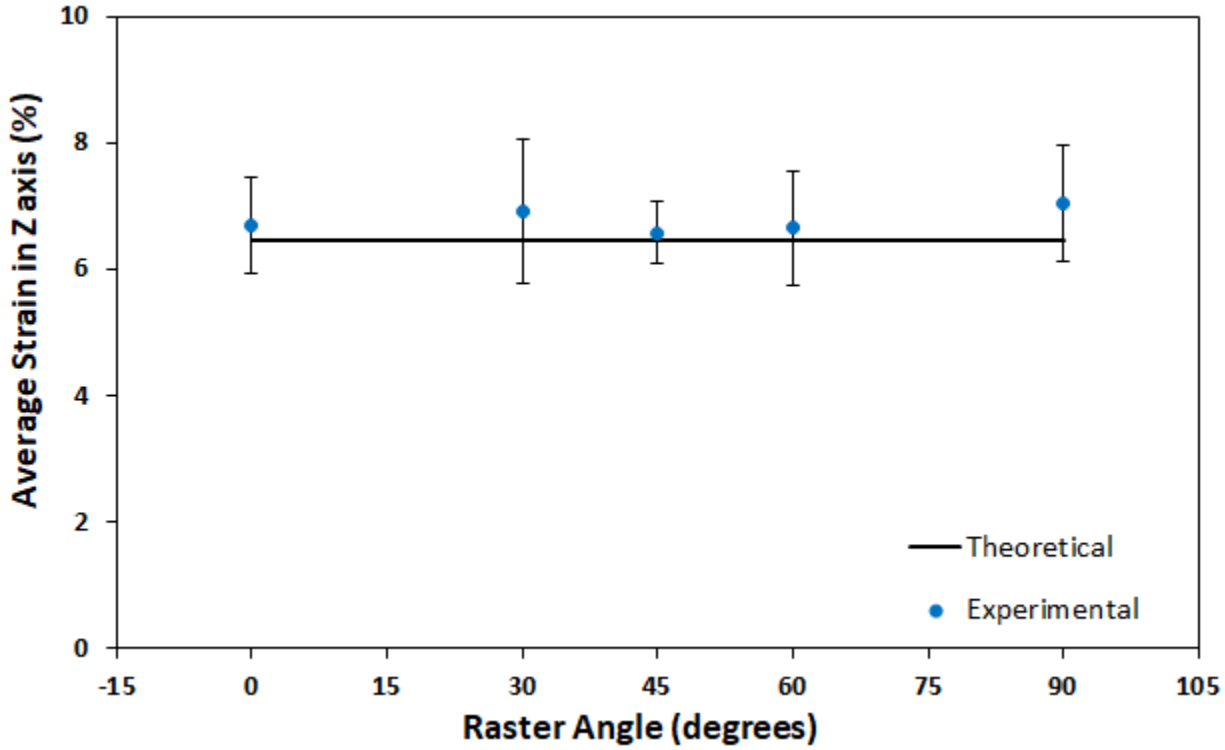

Figure 15: Calculated vs Measured Strain at 140µm in Z axis with error bars representing standard deviation of mean strain of sample set

Experimental strain in the Z axis aligns with the theory; the magnitude and flat trend of data agree with predicted strain.

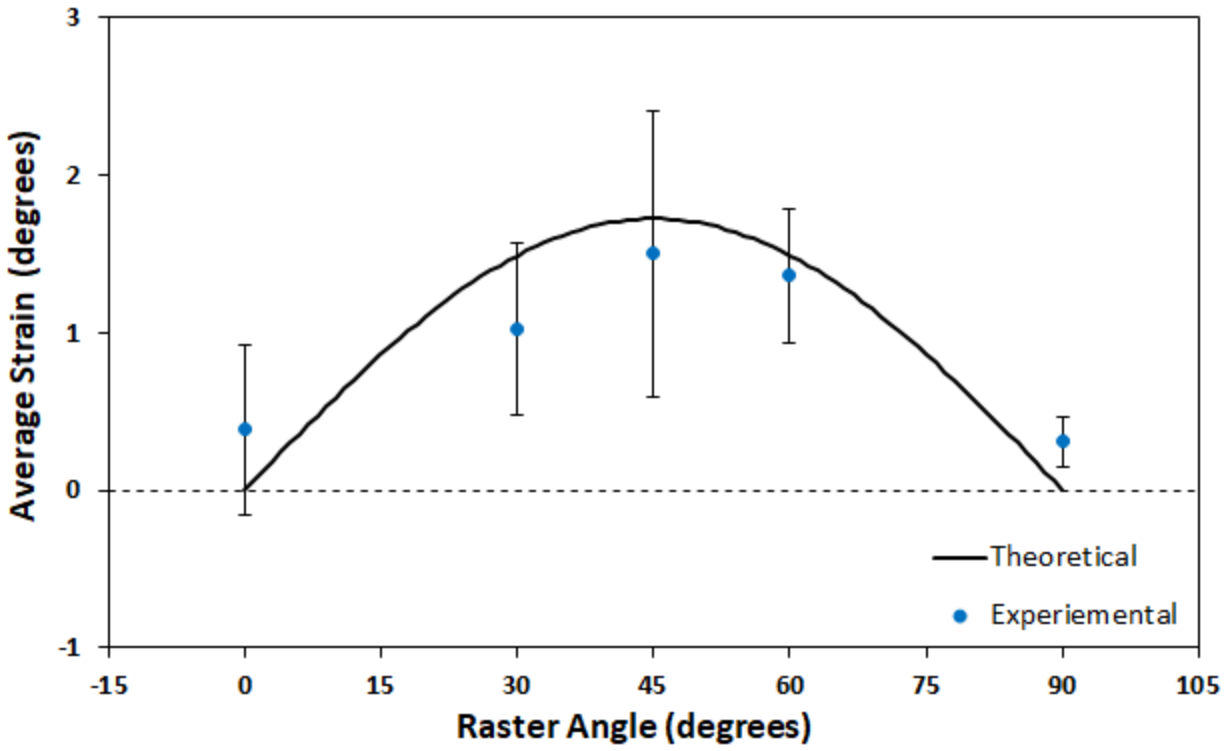

Figure 16: Calculated vs Measured Shear Strain at 140µm with error bars representing standard deviation of mean strain of sample set

Zero shear strain was expected at 0° and 90° raster angles; however, small shear strain values were observed. This deviation was most likely due to experimental error and measurement accuracy error. Given that the error bar at 0° raster angle overlaps with zero, and assuming small values of shear strain observed at 0° and 90° were largely influenced by measurement error caused by warping, the overall trend for observed shear strain follows the predicted trend.

Theoretical and experimental strain at different layer thicknesses were also compared (Figure 17a-d). A majority of the average strain data deviates from the theory by 1-4%, although at times data varied by 5% or more. Despite this, measured strain data in all axes closely follows the trends predicted by the algorithm.

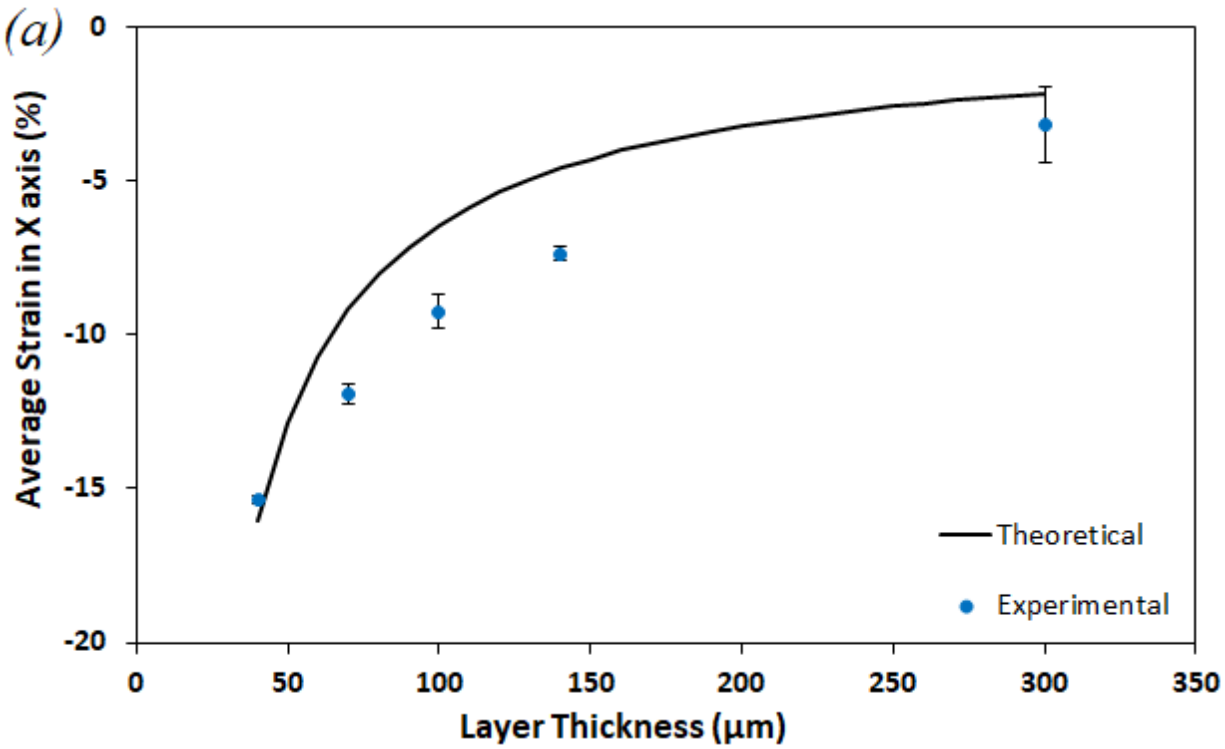
(a)
Average Strain in X axis (%)
0
-5
-10
-15
-20
0
50
100
150
200
250
300
350
Layer Thickness (µm)
Theoretical
Experimental

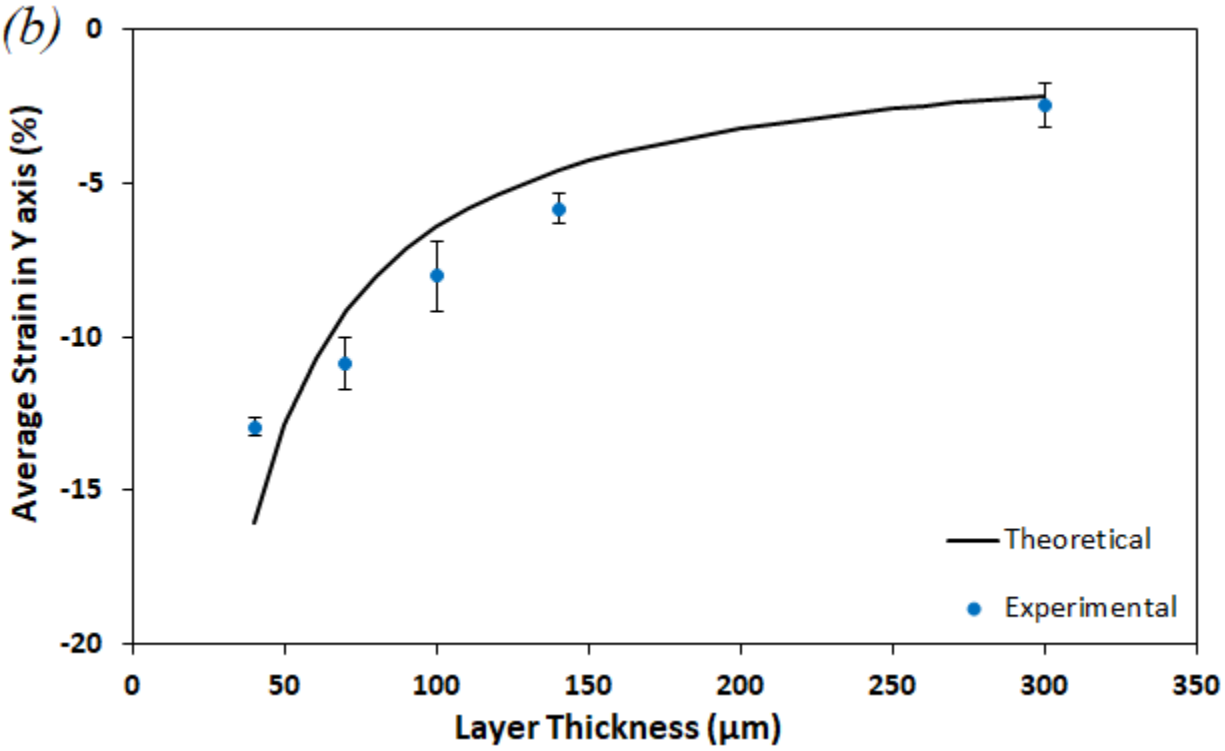
(b)
Average Strain in Y axis (%)
0
-5
-10
-15
-20
0
50
100
150
200
250
300
350
Layer Thickness (µm)
Theoretical
Experimental

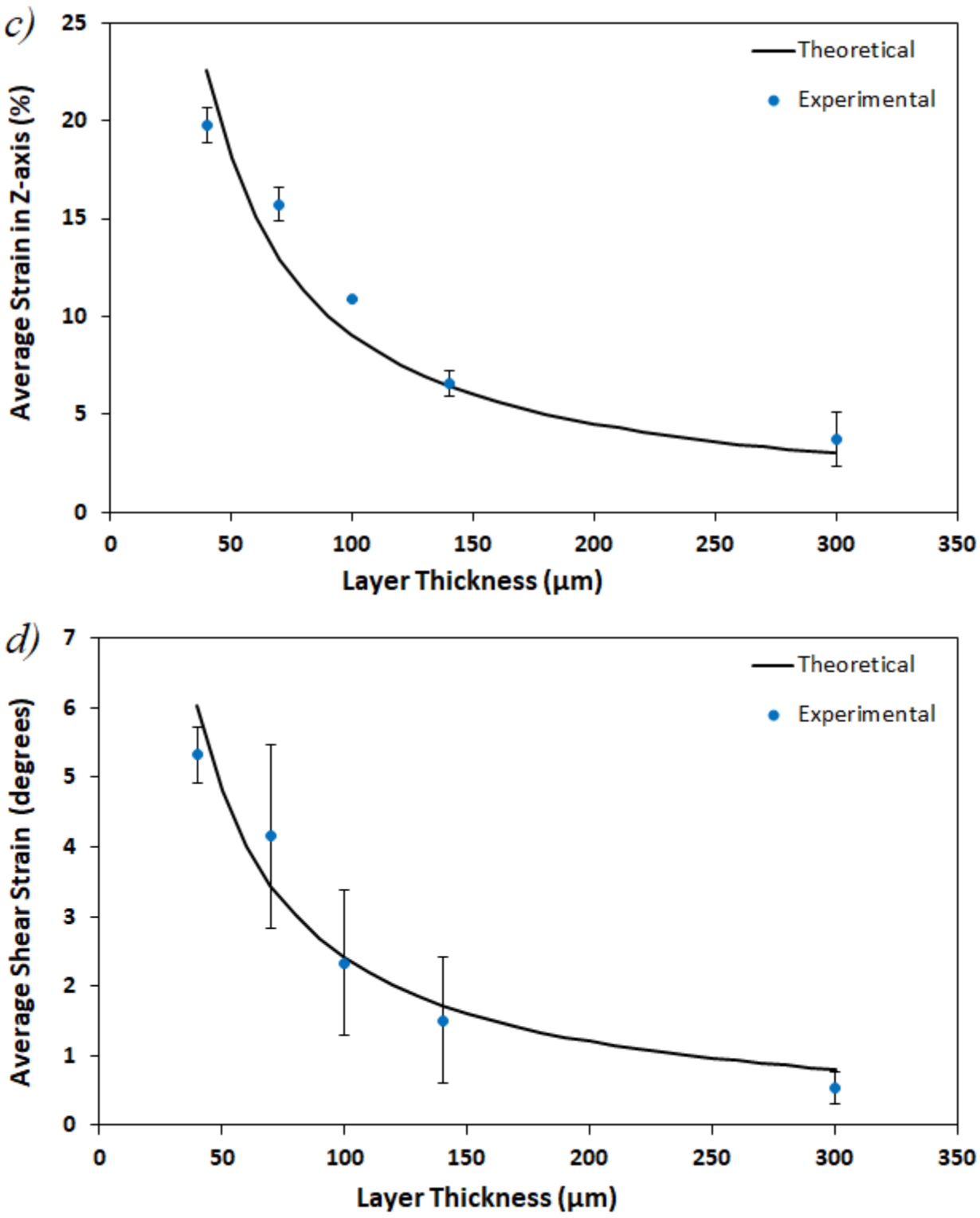

Figure 17: Calculated vs Measured Strain in a) X axis b) Y axis c) Z axis and d) Shear Plane at 45° raster angle with error bars representing standard deviation of mean strain of sample set

Although efforts were made to measure samples with a consistent method, measurement inaccuracy may have caused deviations in data within each sample set. Oftentimes, warping led to over measuring dimensions, as seen in Figure 18 (a) and (b). Twisting and warping were most prevalent at lower layer thickness (Figure 18). A possible explanation may be that lower layer thickness samples require additional layers, and by extension, additional roads. This leads to an increase in road forces. In future research, measurement error may be avoided by setting strict measurement practices that better account for samples with large amounts of warping. Another major error may have been due to non-uniform temperatures within the annealing oven. Strain values for annealed samples with identical print parameters unexpectedly varied, depending on the placement of sample in the oven. Samples annealed in the back of the oven showed greater strain than other samples within each set.

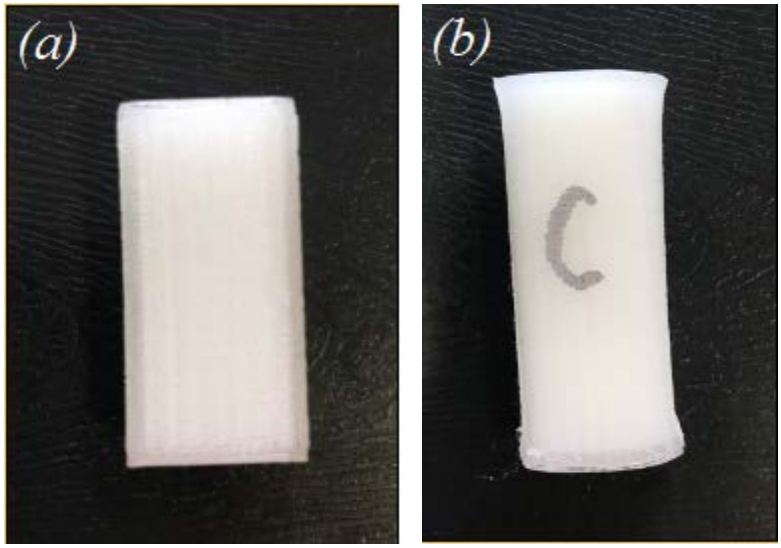

Figure 18: Difference between samples printed at a) 400µm layer thickness and b) at 20µm layer thickness keeping all other printing parameters the same

4.5 Developing Empirical Equations

Deviation of experimental data from theoretical prediction indicates that the algorithm cannot predict resultant strain in 3D printed parts for all polymers. Experimental strain data in X axis and Y axis did not fit the theoretical strain predicted by the algorithm, and so equations of the algorithm were altered. Constants were added to algorithm equations to form empirical models for strain that closely matched experimental results (Equations 13 and 14). Graphical representation is shown in Figures 17 and 18.

$$\varepsilon_x = (F_r/(E * w_r * l_t)) * (cos^2(\theta) - v_{xy}sin^2(\theta)) \text{ -.02} \qquad \textbf{(Equation 13)}$$

$$\varepsilon_y = [(F_r/(E * w_r * l_t)) * [(sin^2(\theta) - v_{xy}cos^2(\theta))\text{*0.3] -.0375} \qquad \textbf{(Equation 14)}$$

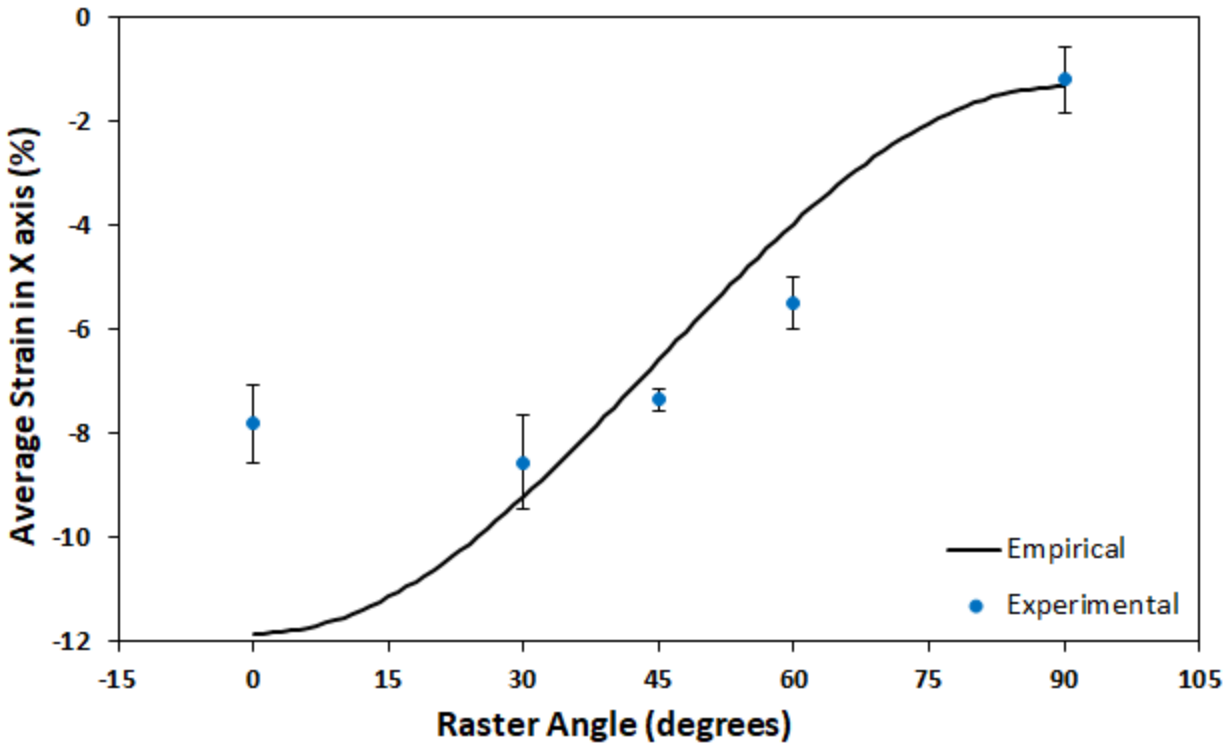

Figure 19: Empirical strain relationship in X axis represented by altered algorithm Equation 13 with error bars representing standard deviation of mean strain of sample set

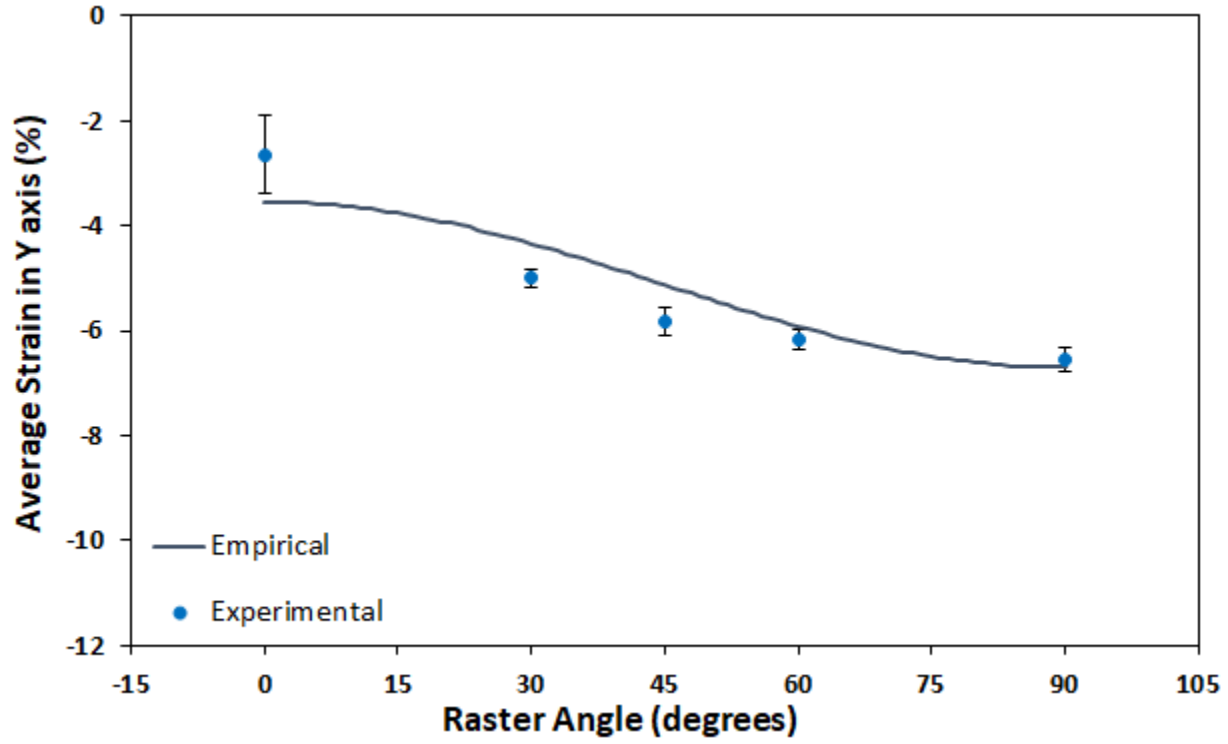

Figure 20: Empirical strain relationship in Y axis predicted by altered algorithm Equation 14 with error bars representing standard deviation of mean strain of sample set

Table 6: Mean square error of theoretical and empirical raster angle strain data

Mean Square Error		
	Theoretical	Empirical
X	0.00295	0.00196
Y	0.00336	0.00018

Constants may represent the effect of crystallinity and density on strain in PLA samples, which are not a factor in ABS. In X and Y strain equations, factors of -0.02 and -0.0375 are added; this means that -2.0% and -3.75% strain are added to X and Y axes theoretical trends to better represent experimental data. Adjusting the empirical trend for Y axis strain also involved damping the curve by multiplying the equation by 0.3. This decreased the predicted strain magnitude, closer fitting the data. Comparison of mean square error (MSE) for both theoretical and empirical fits to the observed data shows that a closer fit was achieved with empirical equations; smaller MSE between observed data and empirical fit in the X and Y axes show this (Table 6).

4.6 Algorithm Verification

Initial printing dimensions to achieve 20x20x20 (mm) in X, Y, and Z axes, respectively, were calculated using Equations 11-14 (Table 3). Evaluation of post-annealed measurements deemed algorithm verification successful in Y and Z axes but not in X (Figure 21). Reason for unsuccessful validation may be because, in previous layer thickness analysis, experimental data in the X axis largely deviated from theoretical at 140μm layer thickness. This result suggests that the empirical relationship for the X axis requires further adjustment to accurately predict strain in parts. Verification of shear strain prediction was not successful. Measured and expected shear strain were 1.25°, and 1.78°, respectively. Shear angle deviation from the expected value was not below the maximum allowable deviation of 0.50°. Discrepancy between target and resultant shear strain (Figure 22) is possibly influenced by trends observed in data in Figure 20, in which experimental values for shear strain at 45° were lower than expected.

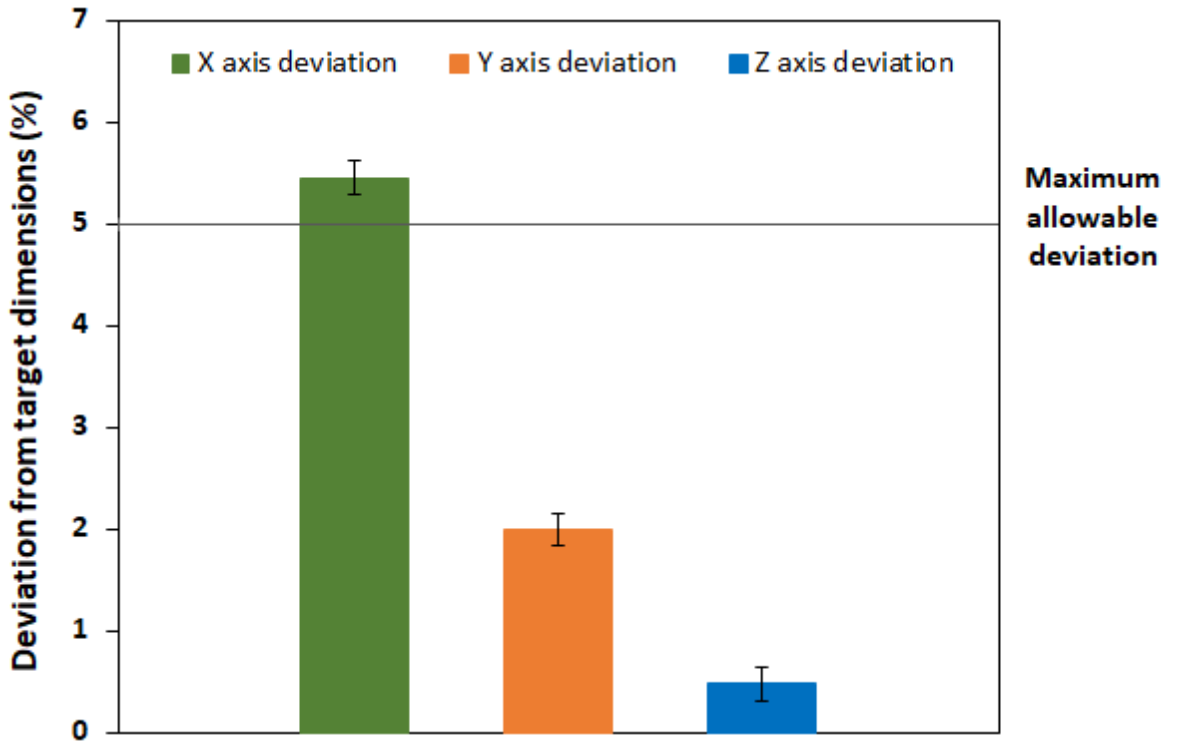

Figure 21: Deviation of samples' dimensions from target dimensions with error bars representing standard deviation of mean strain of sample set

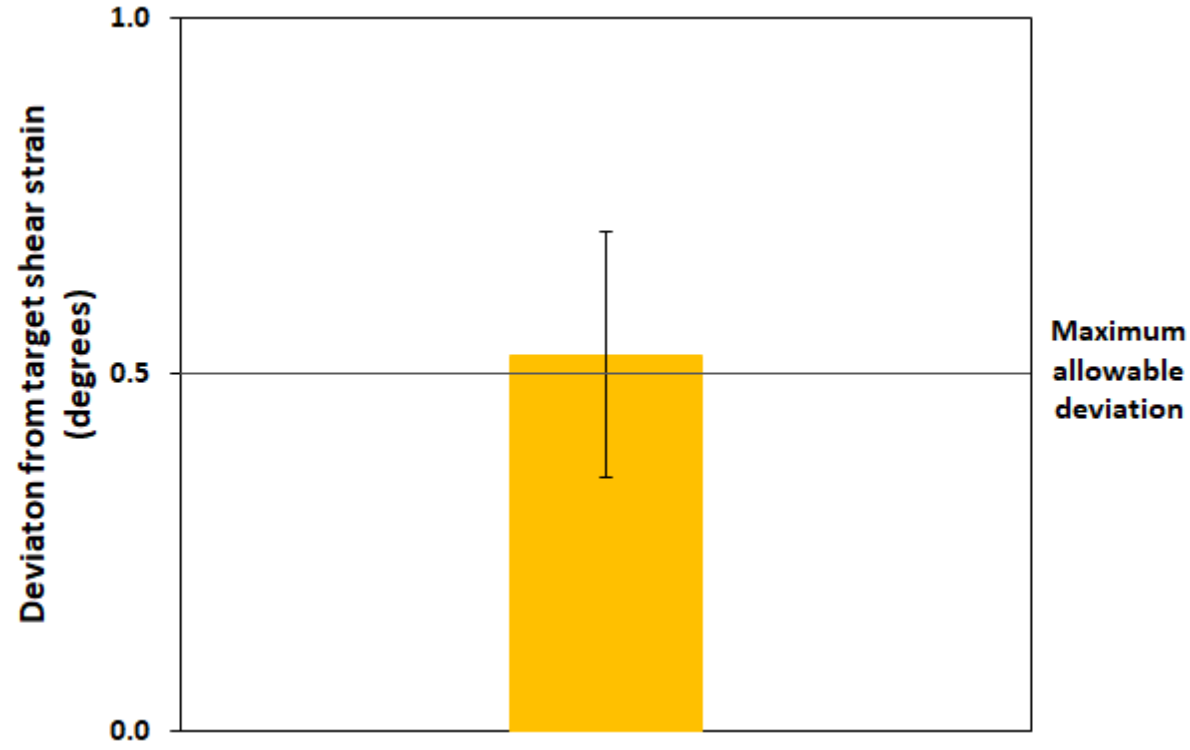

Figure 22: Average shear strain in algorithm verification sample with error bar representing standard deviation of mean strain of sample set

4.7 Effect of Raster Angle on Volumetric Change

Upon completion of the algorithm verification, additional factors were analyzed to explain discrepancies found between empirical and experimental data. Volumetric change in samples, and the effect of varying outline shell thickness were observed.

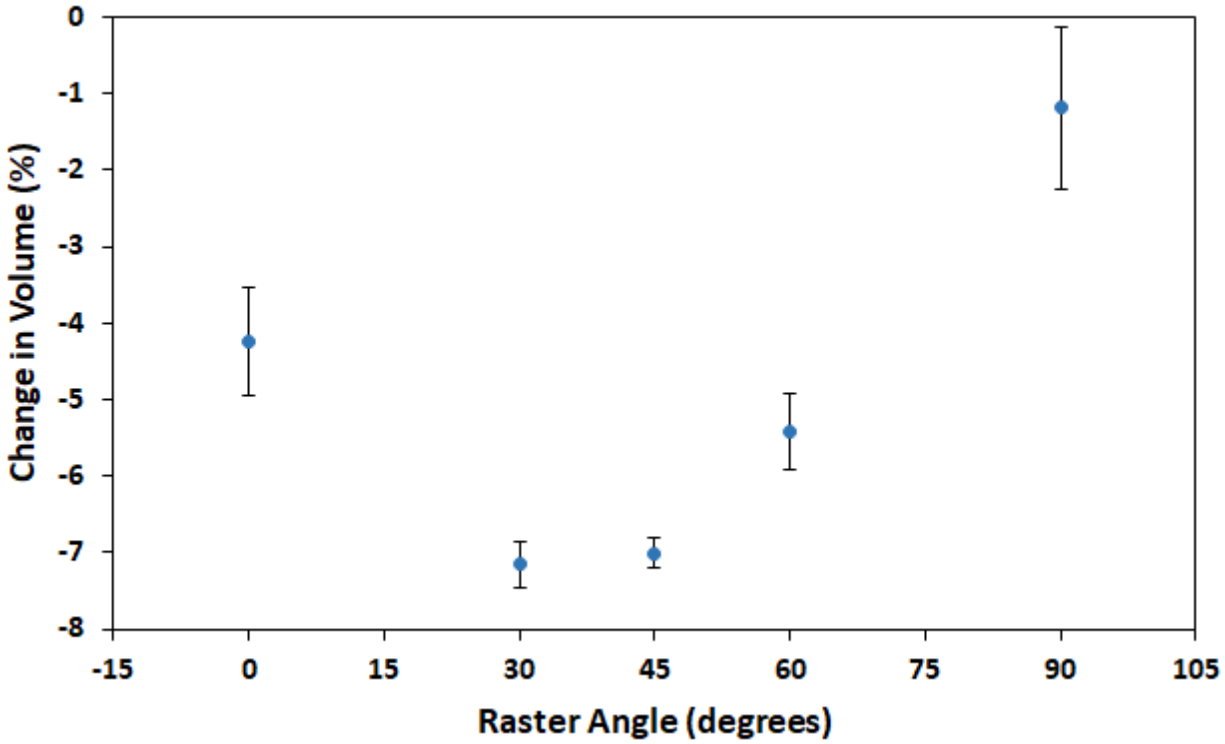

Figure 23: Change in Sample Volume (%) vs. Raster Angle with error bars representing standard deviation of mean strain of sample set

Data in Figure 23 appears to suggest a somewhat erratic pattern of change in volume vs. raster angle, possibly due to measurement error and a crystallinity factor found in strain data for the X and Y axes. The Z axis was not affected by changes in raster angle, and thus was a constant when calculating changes in volume for samples. X axis strain values appeared to be the driving force for percent volumetric change in samples due to both the magnitude, and non-linear nature of the data. Y axis data was more linear, and so caused less overall change in volume. Comparing discrepancies between expected and experimental data in the X and Y axes may explain these trends. Densification by crystallization is a possible explanation for the decrease in sample volume after annealing, although further research is required to determine the extent to which densification drives the observed trends. Crystallization would likely have a consistent effect on volume change in samples, independent of raster angle; based on this, it is believed that additional factors contribute to differences in volume change at different raster angles.

4.8 Effect of Outline Shell

The effect of outline shell was an additional factor considered when testing samples. Outline shell thickness had not been previously analyzed in the context of its individual impact on

resultant strain. Results show an increase in outline shell thickness has a significant impact on inducing strain in samples.

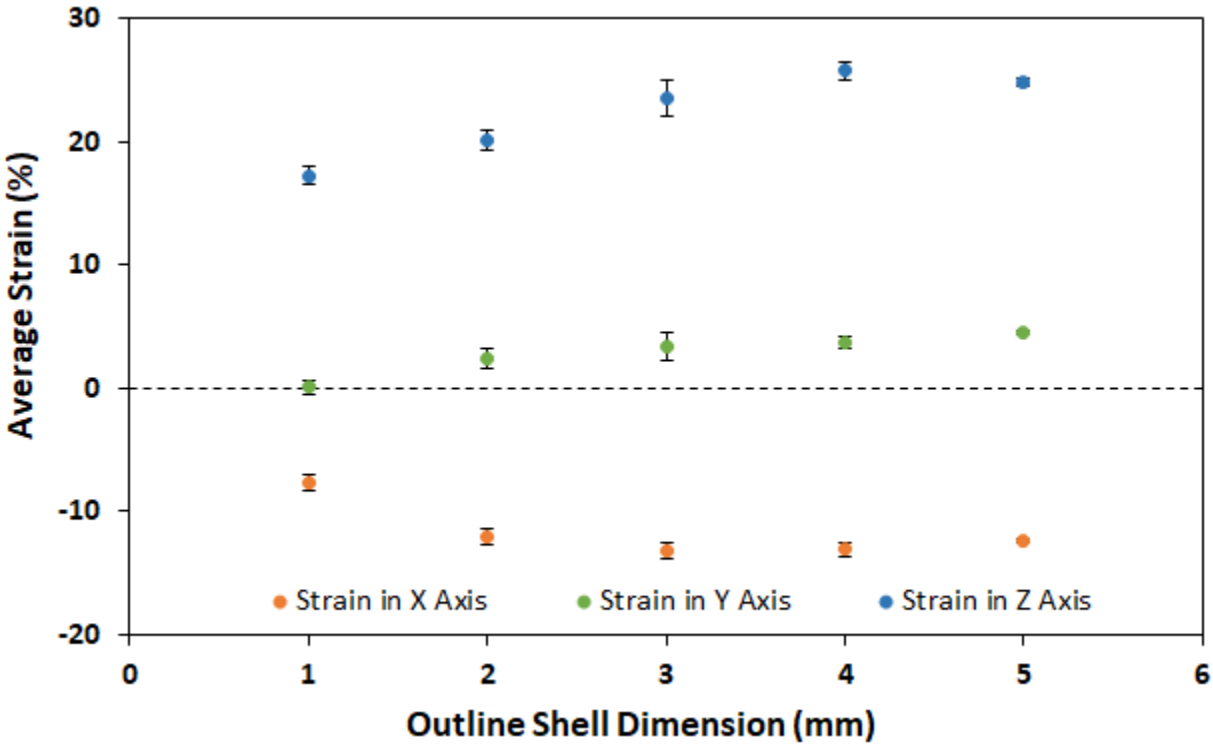

Figure 24: Strain in X, Y, Z axes vs. Outline Shell Dimension with error bars representing standard deviation of mean strain of sample set

Data suggests that the magnitude of strain scales with outline shell thickness of samples (Figure 24). Increasing the size of outline shells correlates with increases in strain in X, Y, and Z axes. However, the strain trend in samples with largest outline shells shows a slight decrease in strain recorded in the X and Z axes. The Z axis experienced largest strain of 26%, following a trend of increasing strain from 1mm to 4mm outline shells before experiencing a slight decrease at an outline shell thickness of 5mm. A similar trend was seen in the X axis. The Y axis also followed a similar trend, however, strain continued to increase up to largest outline shell thickness, unlike in the X and Z axes. It is interesting to note that strain increased in the Y axis, possibly due to increased warping in outline shell samples, affecting measurements.

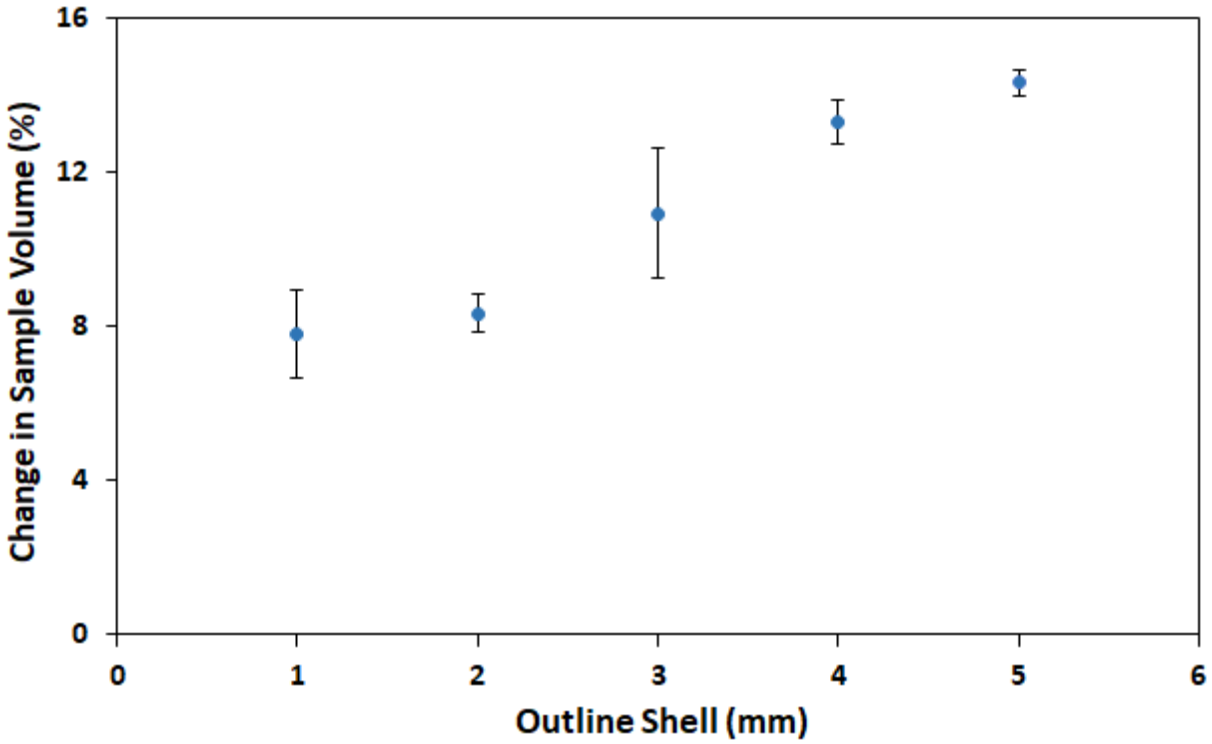

Figure 25: Change in sample Volume (%) vs. Outline Shell (mm) with error bars representing standard deviation of mean strain of sample set

Volumetric change among samples increased with larger outline shell dimension. Data from Figure 25 appear to form a sigmoid (s-shaped) curve. This implies that increasing outline shell thickness between 1mm and 3mm causes samples to expand at an increasing rate due to larger resultant strains within each sample. As outline shell thickness approaches the maximum of 5mm, raster angle dependent road forces may be mitigated through the absence of non-outline shell roads, hence the decreased rate of expansion between 4mm and 5mm. Observations based on Figure 25 indicate that an increase in volume caused by increasing outline shell thickness may correlate with an increase in strain (Figure 24). This data can be used to determine an optimal outline shell thickness that maximizes strain and volume increase before twisting occurs at large outline shell dimensions. Analyzing raster angle's effect on volumetric change and outline shell thickness provided interesting insight, but further research is required to determine if, and how, the empirical algorithm should be adjusted based on the observed trends.

4.9 Challenges with Printing PLA

Initially, samples were printed with a Zortrax M200 3D printer. When printing PLA, the printer frequently became clogged and would jam, making printing samples extremely difficult and results inconsistent. Infill of parts was sometimes sparse, most likely due to the printer's nozzle being clogged with previous polymer or humidity of the environment (Figure 26). PLA absorbs water in the air and degrades more easily at 3D printing temperature as a result. Thorough drying of filament before printing results in improved adhesion and mechanical properties of printed parts

[27]. Attempts were made to reduce jamming during printing by using PLA filament from a different manufacturer, and by printing the filament at different temperatures. However, reliable printing with the Zortrax to create high quality samples was not achieved. The Zortrax 3D printer is designed for much stiffer materials than PLA; the mechanism for feeding the filament into the print head is not optimized for low T_g polymers [29].

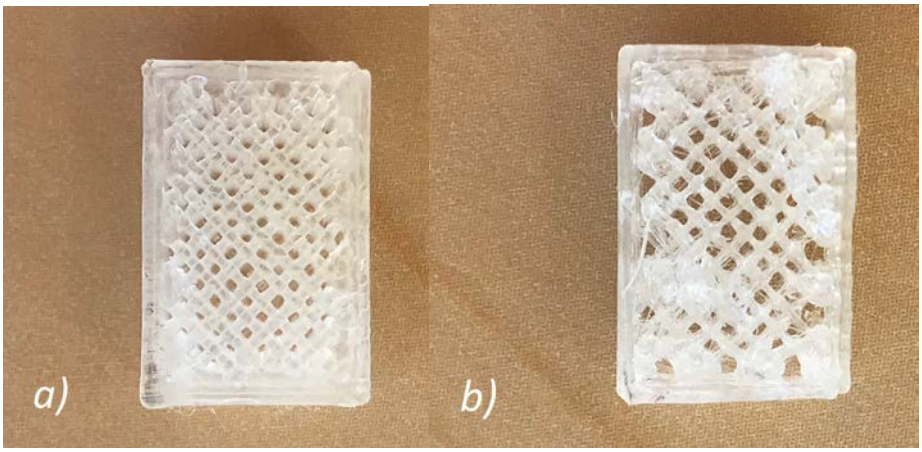

Figure 26: Samples printed by Zortrax with maximum infill percentage a) higher quality, denser sample b) lower quality, sparse infill

Printing PLA with the Zortrax also resulted in large dimensional inaccuracy in some models (Figure 27). It's possible that the Zortrax could not determine its positioning during printing relative to the model, causing it to misalign layers early in the print. Challenges during printing made it impossible to achieve timely results for testing and so a decision was made to print samples with an Ultimaker 3 3D printer.

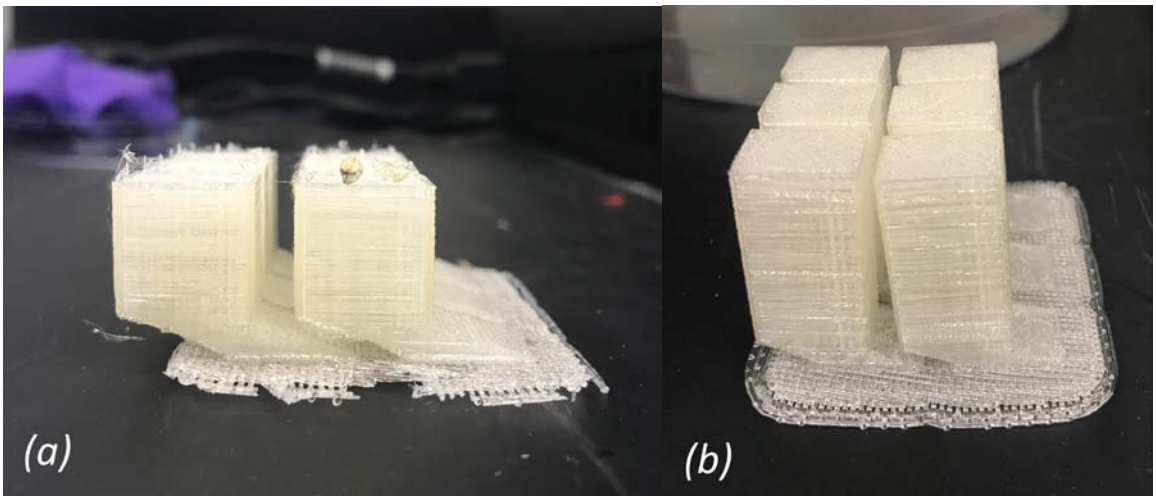

Figure 27: a) Incomplete and misaligned sample print by the Zortrax M200 b) Complete but misaligned sample print by the Zortrax M200

5. Conclusions

The purpose of this research was to verify the use of a 3D printing algorithm in predicting irreversible thermal strain for PLA, and determine effects of outline shells on strain in 3D printed parts. While linear strain in the Z axis and shear strain in the XY-plane are well represented by the developed algorithm, strain in the X and Y axes did not align with theory. Discrepancies with data were largely influenced by the difficulty of accounting for warping when measuring samples. However, it is also possible that an unaccounted for factor affected irreversible thermal strain in the X and Y axes. A possible factor is the semi-crystalline nature of 3D printed PLA.

After deviations between theoretical and experimental trends were observed, an empirical relationship for strain in the X and Y axes was developed. The addition of empirical constants, as well as a proportionality constant to dampen the Y equation, provided a better fit to observed data. Respective empirical and theoretical equations were successful at predicting strain in the shear plane, and in Y and Z axes, but not in X. This suggests that the empirical equation representing strain in the X axis was not a close enough fit for all data points.

Analysis of the relationship between outline shell thickness and strain showed an increasing trend in strain magnitude in X, Y and Z axes up to 4 mm outline shell thickness. However, samples printed with maximum outline shell of 5mm did not achieve the largest strain, suggesting a limit to the strain induced by outline shell. Samples with larger outline shells displayed more pronounced warping; this indicated that an optimal outline shell dimension for observing shape transformation may be achieved by selecting a thickness that maximizes strain while mitigating warping. Outline shell testing provided useful information for future research in MatEx.

The main factor influencing observed strain data was the bulging effect that occurred in printed samples. In future research, the effect of warping on strain measurements can be mitigated by avoiding measuring the centers of samples with calipers. Another way to address warping is to ensure that a consistent temperature is used during annealing. Other factors affecting observed strain could be due to crystallinity of PLA, or 3D printing parameters. Otherwise, this research mostly agreed with trends in strain seen in previous research conducted with ABS. The printing algorithm can be refined with further analysis of the independent effect of outline shell on strain in parts, adding another factor to consider when determining final part dimensions. These studies could help to determine an accurate empirical relationship for strain in the X axis. Development of a universal 3D printing algorithm for polymers is valuable as MatEx becomes increasingly popular as a manufacturing technique. A consistent and reliable MatEx printing algorithm could advance manufacturing processes and open new avenues of developing SMP applications across industry, particularly in the aerospace and biomedical industries.

References

(1) do Nascimento, R. O.; Chirani, N. 13 - Shape-Memory Polymers for Dental Applications. In *Shape Memory Polymers for Biomedical Applications*; Yahia, L., Ed.; Woodhead Publishing Series in Biomaterials; Woodhead Publishing, 2015; pp 267–280.

(2) Can Shape Memory Polymer Hybrids Be Used for Smart Automotive Body Panels? | Society of Plastics Engineers https://www.4spe.org/Resources/resource.aspx?ItemNumber=5185 (accessed Feb 13, 2018).

(3) Sokolowski, W.; Metcalfe, A.; Hayashi, S.; Yahia, L.; Raymond, J. Medical Applications of Shape Memory Polymers. Biomed. Mater. 2007, 2 (1), S23.

(4) David Bak, (2003) "Rapid prototyping or rapid production? 3D printing processes move industry towards the latter", Assembly Automation, Vol. 23 Issue: 4, pp.340-345, https://doi.org/10.1108/01445150310501190

(5) Savini, A. Savini, G.G. (2015) “A short history of 3D printing” http://ieeexplore.ieee.org/xpls/icp.jsp?arnumber=7307314.

(6) McIlroy, Claire, and Peter D. Olmsted. “Deformation of an Amorphous Polymer during the Fused-Filament-Fabrication Method for Additive Manufacturing.” *Journal of Rheology* 61.2 (2017): 379–397. *arXiv.org*. Web.

(7) Material Extrusion | Additive Manufacturing Research Group | Loughborough University http://www.lboro.ac.uk/research/amrg/about/the7categoriesofadditivemanufacturing/materialextrusion/ (accessed Sep 26, 2017).

(8) *3D Printing Guide: 6 Steps (with Pictures)*, http://www.instructables.com/id/3D-Printing-101-1-Introduction/ (accessed Mar 15, 2018).

(9) MakerBot *Makerbot 2X replicator User Manual* 2012**,** http://downloads.makerbot.com/replicator2x/MakerBot_Replicator_2X_User_Manual.pdf (accessed Sep 27, 2017)

(10) Sun, Q., et al. "Effect of Processing Conditions on the Bonding Quality of FDM Polymer Filaments." *Rapid Prototyping Journal* 14.2 (2008): 72-80. *ProQuest.* Web. 26 Sep. 2017.

(11) 2017 Best 3D Printer Guide https://www.3dhubs.com/best-3d-printer-guide (accessed Sep 26, 2017).

(12) D’Amico, A. A.; Debaie, A.; Peterson, A. M. Effect of Layer Thickness on Irreversible Thermal Expansion and Interlayer Strength in Fused Deposition Modeling. *Rapid Prototype. J.* 2017, *23* (5).

(13) Barrett, C.; Presing, J.; D’Amico, A. A.; Peterson, A. One-Way 3D Printed Shape Memory Polymers

(14) Ultimaker *Ultimaker 3 User Manual* 2016, https://ultimaker.com/download/61355/Ultimaker%203%20manual%20%28EN%29.pdf (accessed Sep 27, 2017)

(15) Z-SUITE Manual http://support.zortrax.com/z-suite-manual/ (accessed Sep 26, 2017).

(16) Understanding the Rheological Characteristics of Thermoplastic Polymers https://www.azom.com/article.aspx?ArticleID=12100 (accessed Oct 10, 2017).

(17) Callister, W.; Rethwisch, D. Materials Science and Engineering, 7th ed.; John Wiley & Sons, Inc, 2007.

(18) Granta. CES EduPack 2017 PLA (general purpose).

(19) Casavola, C.; Cazzato, A.; Moramarco, V.; Pappalettera, G. In *Residual Stress, Thermomechanics & Infrared Imaging, Hybrid Techniques and Inverse Problems, Volume 9*; Conference Proceedings of the Society for Experimental Mechanics Series; Springer, Cham, 2017; pp 91–96.

(20) Wang, T.-M.; Xi, J.-T.; Jin, Y. *Int J Adv Manuf Technol* 2007, *33* (11–12), 1087–1096.

(21) Kantaros, A.; Karalekas, D. Fiber Bragg Grating Based Investigation of Residual Strains in ABS Parts Fabricated by Fused Deposition Modeling Process. *Mater. Des.* 2013, *50* (Complete), 44–50.
(22) Dinwiddie, R. B.; Kunc, V.; Lindal, J. M.; Post, B.; Smith, R. J.; Love, L.; Duty, C. E. Colbert, F. P., Hsieh, S.-J. (Tony), Eds.; 2014; p 910502.
(23) Lendlein, A. and Kelch, S. (2002), Shape-Memory Polymers. Angewandte Chemie International Edition, 41: 2034–2057. doi:10.1002/1521-3773(20020617)41:12<2034::AID-ANIE2034>3.0.CO;2-M
(24) Liu, C., H. Qin, and P. T. Mather. "Review of Progress in Shape-Memory Polymers." *Journal of Materials Chemistry* 17.16 (2007): 1543–1558. *pubs.rsc.org*. Web.
(25) Yang, Yang et al. "3D Printing of Shape Memory Polymer for Functional Part Fabrication." *The International Journal of Advanced Manufacturing Technology* 84.9–12 (2016): 2079–2095. *CrossRef*. Web.
(26) Lendlein, Andreas, and Robert Langer. "Biodegradable, Elastic Shape-Memory Polymers for Potential Biomedical Applications." *Science* 296.5573 (2002): 1673–1676. *science.sciencemag.org*. Web.
(27) Gabor, J.; Tabi, T. Biodegradable Polymers Based on Starch and Poly(Lactic Acid). *Plastics Research Online* 2011.
(28) Lohmeijer, P. J. A., Goossens, J. G. P. and Peters, G. W. M. (2016), Quiescent crystallization of poly(lactic acid) studied by optical microscopy and light-scattering techniques. J. Appl. Polym. Sci., 134, 44566. doi: 10.1002/app.44566
(29) Tips for Printing with Z-PLA Pro https://support.zortrax.com/tips-for-printing-with-z-pla-pro/ (accessed Mar 23, 2018).